Remote Sensing of Environment xxx (xxxx) xxx–xxx

Contents lists available at ScienceDirect

Remote Sensing of Environment

journal homepage: www.elsevier.com/locate/rse

Downscaling of solar-induced chlorophyll fluorescence from canopy level to photosystem level using a random forest model

Xinjie Liu[a,b], Luis Guanter[b], Liangyun Liu[a,*], Alexander Damm[c,d], Zbyněk Malenovský[e,f], Uwe Rascher[g], Dailiang Peng[a], Shanshan Du[a], Jean-Philippe Gastellu-Etchegorry[h]

[a] Key Laboratory of Digital Earth Science, Institute of Remote Sensing and Digital Earth, Chinese Academy of Sciences, Beijing 100094, China
[b] Helmholtz Center Potsdam, GFZ German Research Center for Geosciences, Remote Sensing Section, Telegrafenberg A17, 14473 Potsdam, Germany
[c] Remote Sensing Laboratories, Department of Geography, University of Zurich, Winterthurerstrasse 190, 8057 Zurich, Switzerland
[d] Department of Surface Waters – Research and Management, Eawag, Swiss Federal Institute of Aquatic Science and Technology, 8600 Dübendorf, Switzerland
[e] Surveying and Spatial Sciences, School of Technology Engineering and Design, University of Tasmania, Private Bag 76, TAS, 7001 Hobart, Australia
[f] Centre for Sustainable Ecosystem Solutions, School of Biological Sciences, University of Wollongong, NSW, 2522 Wollongong, Australia
[g] Institute of Bio- and Geosciences, IBG-2: Plant Sciences, Forschungszentrum Jülich, Leo-Brandt-Str., 52425 Jülich, Germany
[h] Toulouse University, CESBIO, CNRS, CNES, IRD, Paul Sabatier University, Toulouse, France

ARTICLE INFO

Keywords:
Solar-induced chlorophyll fluorescence
Downscaling
Canopy level
Photosystem level
Spectral invariant theory
Random Forest regression

ABSTRACT

Solar-induced chlorophyll fluorescence (SIF), an electromagnetic signal that can potentially indicate vegetation photosynthetic activity, can be retrieved from ground-based, airborne and satellite measurements. However, due to the scattering and re-absorption effects inside the leaves and canopy, SIF measured at the canopy level is only a small part of the total SIF emission at the photosystem level. Therefore, a downscaling mechanism of SIF from the canopy level to the photosystem level is important for better understanding the relationship between SIF and the vegetation gross primary production (GPP). In this study, firstly, we analyzed the canopy scattering effects using a simple parameterization model based on the spectral invariant theory. The probability for SIF photons to escape from the canopy was found to be related to the anisotropic spectral reflectance, canopy interception of the upward solar radiation, and leaf absorption. An empirical approach based on a Random Forest (RF) regression algorithm was applied to downscale SIF constrained by the red, red-edge and far-red anisotropic reflectance. The RF was trained using simulations conducted with the Soil Canopy Observation, Photochemistry and Energy fluxes (SCOPE) model. The performance of the SIF downscaling method was evaluated with SCOPE and Discrete Anisotropic Radiative Transfer (DART) model simulations, ground measurements and airborne data. Results show that estimated SIF at the photosystem level matches well with simulated reference data, and the relationship between SIF and photosynthetically active radiation absorbed by chlorophyll is improved by SIF downscaling. This finding in combination with other evaluation criteria suggests the downscaling of canopy SIF as an efficient strategy to normalize species dependent effects of canopy structure and varying solar-view geometries. Based on our results for the SIF-APAR relationship, we expect that such normalization approaches can be helpful to improve estimates of photosynthesis using remote sensing measurements of SIF.

1. Introduction

Solar-induced chlorophyll fluorescence (SIF) has been proved to be an efficient tool for monitoring of gross primary production (GPP), showing large advantages compared with other remote sensing indicators based on reflectance-data (Guanter et al., 2014; Migliavacca et al., 2017; Porcar-Castell et al., 2014; Sun et al., 2017; Zhang et al., 2016). The photosynthetically active energy absorbed by leaf pigments can be: i) used in photochemical reactions, ii) dissipated as heat, or iii) re-emitted as fluorescence (Porcar-Castell et al., 2014). Unlike the reflectance based parameters, SIF is, as a by-product of photosynthesis, more directly related to GPP (Berry et al., 2012; Coops et al., 2010; Damm et al., 2015a; Zarco-Tejada et al., 2013).

Validity of the resource balancing paradigm (Field et al., 1998) in combination with the Monteith light use efficiency (LUE) model (Monteith, 1972; Monteith and Moss, 1977) is the foundation of most of the approaches for the estimation of GPP from remote sensing data. The LUE model can be expressed as:

$$GPP = PAR \times fAPAR \times LUE \quad (1)$$

* Corresponding author at: No.9 Dengzhuang South Rd., Haidian, Beijing 100094, China.
E-mail address: liuly@radi.ac.cn (L. Liu).

https://doi.org/10.1016/j.rse.2018.05.035
Received 15 January 2018; Received in revised form 25 May 2018; Accepted 31 May 2018

where PAR stands for the photosynthetically active radiation, fAPAR is the fraction of PAR absorbed by vegetation, and LUE is the light use efficiency, defined as the number of μmol of CO_2 absorbed per μmol of photons.

Similarly, the total SIF emission at the photosystem (PS) level (the total SIF emission inside the leaves without any scattering or re-absorption) can be expressed as (Berry et al., 2012; Liu et al., 2017a, b; Moya and Cerovic, 2004; Porcar-Castell et al., 2014; Wieneke et al., 2016):

$$SIF_{PS}(\lambda) = PAR \times fAPAR \times F_{yield}(\lambda) \quad (2)$$

where λ is the wavelength, and F_{yield} is the quantum yield for chlorophyll fluorescence. If F_{yield} is constant, then SIF_{PS} is linearly related to the PAR absorbed by vegetation.

In recent years, we have been experiencing a rapid development of methods for SIF retrieval from spectral remote sensing data (Malenovský et al., 2009). The SIF signal can be detected by ground-based (Grossmanna, 2014; Liu et al., 2005, 2017a; L. Liu et al., 2015; X. Liu et al., 2015; Wyber et al., 2017; Yang et al., 2015; Cogliati et al., 2015; Burkart et al., 2015), airborne (Damm et al., 2014; Rascher et al., 2015; Wieneke et al., 2016), and space-borne sensors (Frankenberg et al., 2011; Guanter et al., 2012; Joiner et al., 2011, 2013; Köhler et al., 2015). However, SIF is emitted by chlorophyll *a* molecules, which are contained inside chloroplasts at different leaf mesophyll layers. Re-absorption and scattering of SIF are both taking place inside leaves as well as within the canopy. Using remote sensing approaches at large scales, it is only possible to measure SIF at the canopy level (SIF_{Canopy}, defined as SIF escaping from the canopy in a specific viewing direction).

The SIF spectrum extends over the wavelength range from about 640 to 850 nm, with two peaks centered at 685 nm and 740 nm. Ramos and Lagorio (2004) pointed out that the spectral shape of fluorescence measured at leaf level was influenced by the leaf re-absorption, and developed a model to correct the spectral shape using leaf reflectance. Van Wittenberghe et al. (2015) studied the upward and downward SIF emission at the leaf level separately using a special leaf probe called FluoWat, and found that the partitioning of the upward and downward SIF components is influenced by scattering and absorption processes related to the leaf structure and the pigment content. This indicates that the red SIF at 685 nm is strongly influenced by chlorophyll absorption within the leaves, while far-red SIF is mainly influenced by scattering effect of leaf tissue structures. Several studies have reported a decrease in the red/far-red SIF ratio from leaf level to canopy level (Fournier et al., 2012; Moya et al., 2006; Romero et al., 2018), which can be, besides the environmental stress exposure (Ač et al., 2015), explained by the strong re-absorption of SIF by chlorophyll at the red band (Daumard et al., 2012; Fournier et al., 2012; Agati et al., 1993; Cordón and Lagorio, 2006; Porcar-Castell et al., 2014; Romero et al., 2018). Liu et al. (2016) observed similar anisotropic characteristics for SIF and reflectance at the canopy level, and claimed that the phenomenon can be attributed to re-absorption by canopy components and the bidirectional canopy gap fraction. Other studies also reported a similar anisotropic effect for SIF retrieved from space (e.g. Guanter et al., 2012; Joiner et al., 2012), while He et al. (2017) proved that an angular normalization of SIF strengthens SIF-GPP relationships. Further, Du et al. (2017) reported a species-dependent relationship between SIF_{Canopy} and PAR absorbed by chlorophyll ($APAR_{chl}$), and pointed out that the uncertainty in the SIF escape probability weakens the relationship between SIF and $APAR_{chl}$ or GPP, especially at the red band. Therefore, downscaling of SIF from canopy level to PS level is important to better constrain estimates of GPP using remote sensing observations of SIF.

There are two very recent studies focusing on the problem of SIF downscaling. Romero et al. (2018) developed a physical model based on the canopy reflectance, canopy transmittance and soil reflectance to correct the spectral shape of fluorescence emission from canopy level to leaf level. Together with the study by Ramos and Lagorio (2004), the fluorescence spectral shape at PS level could also be retrieved. However, the absolute SIF intensity was not available. Yang and Van der Tol (2018) linked the canopy scattering of far-red SIF to the canopy reflectance, canopy interceptance and leaf albedo based on canopy radiative transfer analysis, but the model was not valid for the red band and the input parameters were not easy to be accurately measured or estimated. Moreover, the SIF downscaling from leaf level to PS level was not included.

Given the fact that the radiative transfer of emitted SIF within a canopy is similar to that for scattered solar radiation, it can be assumed that the modelling of top-of-canopy (TOC) spectral reflectance can approximate the canopy effects on SIF, which is needed for the estimation of SIF escape probability from PS level to canopy level (ε_{CP}) (Van der Tol et al., 2009; Liu et al., 2016). To express the radiative transfer equation within the canopy together with the leaf scattering coefficient, Knyazikhin et al. (1998) introduced a spectral invariant *p*, which was defined by Smolander and Stenberg (2005) as photon recollision probability. Another spectral invariant, bi-directional gap fraction, was introduced to quantify the probability of scattered photons to escape the canopy via gaps in the direction of viewing (Huang et al., 2007; Knyazikhin et al., 2011). The so-called 'spectral invariant theory' has been successfully used to better understand the absorption and scattering effects within the canopy and also to link the reflectance at the canopy level and leaf level (Huang et al., 2007; Knyazikhin et al., 2013; Smolander and Stenberg, 2005; Stenberg et al., 2016; Wang et al., 2003). Similarly, the spectral invariant theory can be applied to model the escape probability for SIF with a number of parameters describing the leaf optical properties, canopy structure, and background reflectance. However, these parameters are usually difficult to accurately measure or estimate. Moreover, spectral invariant theory can only model the radiative transfer process from leaf level to canopy level, while SIF is emitted from inside the leaves, which means that the re-absorption of SIF photons within the leaves (leaf internal absorption) is not accounted for. Although the canopy reflectance also contains information about the leaf absorption, it is difficult to directly link this to the SIF absorption inside the leaves.

Supervised machine learning approaches trained on appropriate training dataset are capable of building accurate prediction models (Ma et al., 2014) that can empirically overcome the difficulties in the physical modelling described above (the unavailable input parameters for the physical model can be estimated by machine learning approaches using available information). The physically based analysis of the radiative transfer process is, in turn, able to point out the appropriate input parameters used in the machine learning methods.

This study aims to define and evaluate a practical solution for the downscaling of SIF from the canopy level to the PS level. The SIF radiative transfer within canopy and inside leaves is analyzed based on the spectral invariant theory and leaf-level simulations to define the key parameters driving the SIF downscaling from canopy level to leaf and PS levels. We then employ an empirical approach based on random forest (RF) regression (Breiman, 2001) to predict the SIF escape probability from leaf level to canopy level (ε_{CL}) and from PS level to canopy level (ε_{CP}) using reflectance information. The Soil Canopy Observation, Photochemistry and Energy fluxes (SCOPE) model (Van der Tol et al., 2009) was then used for the simulation of the training dataset. Finally, we evaluate the performance of the SIF downscaling using SCOPE and Discrete Anisotropic Radiative Transfer (DART) model simulations, ground and airborne data. The presented approach facilitates the normalization of SIF observations across canopy types observed under varying sun-view geometries, and eventually improves our understanding on the relationship between SIF emission and photosynthetic activity.

2. Materials and methods

2.1. Simulated datasets

2.1.1. SCOPE simulation

The SCOPE model (Van der Tol et al., 2009) is a vertical (1-D) integrated radiative transfer and energy balance model, which is able to simulate leaf and canopy spectral reflectance and SIF as well as photosynthesis and water and heat flux by linking the radiative transfer with micro-meteorological processes. SCOPE has been widely used in the field of SIF research (e.g. Verrelst et al., 2015; Zhang et al., 2016; Yang and Van der Tol, 2018). The latest version of SCOPE (v1.7) provides users with SIF at canopy level, leaf level (SIF emitted by all leaves, excluding the re-absorption and scattering within the canopy) and at PS level (SIF emitted by all photosystems, excluding the re-absorption within the leaves). Therefore, we used SCOPE v1.7 for the simulation of SIF at the canopy, leaf and PS levels, along with that of the canopy directional reflectance, leaf reflectance and transmittance.

In the SIF emission spectral range (~640–850 nm), the amount of absorption by leaves is mainly related to chlorophyll content (Jacquemoud and Baret, 1990). The canopy scattering is mainly related to the canopy structure parameters (leaf area index (LAI), leaf inclination distribution, etc.) and solar-view geometries (solar zenith angle (SZA), view zenith angle (VZA) and relative azimuth angle (RAA)) (Verhoef, 1984). We parameterized SCOPE for sets of different leaf chlorophyll contents (Cab), LAI levels and six typical leaf inclination distributions to cover most common vegetation conditions. Additionally, different SZAs and VZAs in the solar principal plane were also defined. The full-width-at-half-maximum spectral response (FWHM) and spectral sampling interval (SSI) for the SCOPE simulations are 1 nm. Details about the SCOPE input parameters are listed in Table 1. As a result, 6240 different samples were generated.

2.1.2. DART simulation

DART is a three-dimensional (3-D) radiative transfer model that allows simulating the radiation budget as well as remotely sensed images of natural and urban surfaces covering the range from the ultraviolet to the thermal infrared band (Gastellu-Etchegorry et al., 2015). Recently, a SIF module that allows simulations of SIF radiative transfer within 3-D canopies has been added to DART (Gastellu-Etchegorry et al., 2017). Similar to SCOPE, DART uses the Fluspect model (Vilfan et al., 2016) to simulate the reflectance, transmittance and SIF emission at the leaf level. In this study, the DART model (v5.6.6) was employed to simulate SIF at both the canopy and leaf levels, together with the directional reflectance of 50 different viewing angles for two geometrically explicit and architecturally different canopies of maize (*Zea mays* L.) and Norway spruce (*Picea abies/L./H. Karst.*). The DART parameterization details are listed in Table 2. Fig. 1 shows the simulated multi-angular SIF at canopy level for maize and spruce at the far-red (740 nm) and red bands (687 nm).

Table 1
Main input parameters for the SCOPE simulations.

Parameter	Values	Unit	Description
C_{ab}	20, 40, 60, 80	μg/cm^2	Leaf chlorophyll $a + b$ content
C_{dm}	0.012	g/cm^2	Dry matter content
C_w	0.009	cm	Leaf water equivalent layer
N	1.4	–	Leaf mesophyll scattering parameter
LAI	1, 2, 3, 4	m^2/m^2	Leaf area index
LIDF$_a$	1, −1, 0, 0, −0.35, 0	–	Leaf inclination parameter
LIDF$_b$	0, 0, −1, 1, −0.15, 0	–	Bimodality parameter
FQE	0.01	–	Fluorescence quantum yield efficiency
SZA	20, 30, 40, 50, 60	Degree	Solar zenith angle
VZA	0, 10, 20, 30, 40, 50, 60	Degree	View zenith angle
RAA	0, 180	Degree	Relative azimuth angle

Table 2
Major input parameters for the DART simulations of maize and spruce canopies.

Parameter	Values	Unit	Description
C_{ab}	58	μg/cm^2	Leaf chlorophyll $a + b$ content
C_{dm}	0.0037	g/cm^2	Dry matter content
C_w	0.0131	cm	Leaf water equivalent layer
N	1.518	–	Leaf mesophyll scattering parameter
LAI	4 (maize), 7 (spruce)	m^2/m^2	Leaf area index
Canopy height	2.25 (maize), 10 (spruce)	m	Canopy height
FQE (PSI)	0.002	–	Fluorescence quantum yield efficiency for photosystem I
FQE (PSII)	0.008	–	Fluorescence quantum yield efficiency for photosystem II
SZA	37.94	Degree	Solar zenith angle
VZA	15–65	Degree	View zenith angle
SAA	311.89	Degree	Solar azimuth angle
VAA	0–180	Degree	View azimuth angle

2.2. Ground measurements

2.2.1. Multi-species experiments

A dataset comprising ground spectral measurements of different species, acquired at three sites, following three specific experimental settings was used to evaluate the performance of SIF downscaling for different canopy structures.

Spectral measurements of winter wheat (*Triticum*) were carried out on five days at the National Precision Agriculture Demonstration Base located at Xiao Tangshan Farm (XTS, 40°11′N, 116°27′E), north of Beijing, China. Diurnal cycles of radiance measurements (nadir view) were conducted on April 8–9 and 18, 2016, when the growth stages of the winter wheat were jointing and booting, and on November 7 and December 8, 2016 when the growth stages were emergence and tillering, respectively. The leaf inclination distribution function (LIDF) of winter wheat was assumed to be spherical based on a visual inspection.

Measurements of cotton (*Gossypium*) and different kinds of vegetables (i.e. sweet potato (*Ipomoea batatas*), Chinese cabbage (*Brassica rapa pekinensis*), thyme (*Thymus*), pumpkin (*Cucurbita Cucurbita*)) were carried out on December 18, 2016 at Nanbin Farm (NBF, 18°22′N, 109°10′E) in Hainan Province, China. The LIDF types of the vegetables and cotton are mostly close to planophile based on visual assessment. For convenience, the term 'vegetables' is used to represent all the species on this site (including cotton).

Diurnal measurements of gold coin grass (*Lysimachiae Herba*) were also carried out on December 18, 2016 at the Sanya Remote Sensing Satellite Data Receiving Station (SYS, 18°18′N, 109°18′E) in Hainan Province, China. The LIDF of this grass was assessed to be close to planophile by visual inspection.

Details of the multi-species measurements described above are summarized in Table 3. All the spectral measurements were conducted using a customized Ocean Optics QE Pro spectrometer (Ocean Optics, Dunedin, FL, USA), characterized by a FWHM of 0.31 nm, a SSI of 0.155 nm, and a peak signal-to-noise ratio (SNR) higher than 1000. For more details of the experiments, please refer to Du et al. (2017).

2.2.2. Multi-angular experiments

Due to the influence of the canopy structure (i.e. variable gap fraction and LIDF), SIF at the canopy level is anisotropic. To test the performance of the SIF downscaling algorithm, we carried out a series of multi-angular measurements on a winter wheat canopy during the springs of 2015 and 2016 at the Xiao Tangshan Farm, Beijing, China, using a multi-angular observation system (MAOS) (Yan et al., 2012).

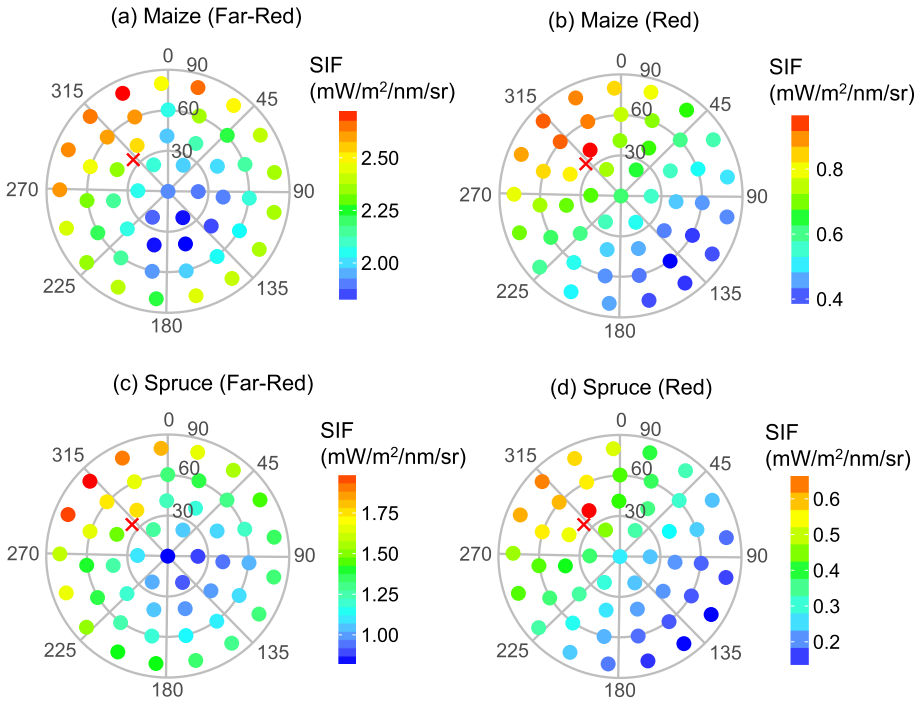

Fig. 1. Multi-angular SIF at canopy level for maize and spruce at the far-red (740 nm) and red (687 nm) bands, as simulated by DART. The labels are the view azimuth (0°–360°, 0° for the north) and zenith (0°–90°) angles. The red cross indicates the solar position (zenith angle: 37.94°; azimuth angle: 311.89°). The incident PAR is 1185.76 W/m^2, and the temperature is 300 K. (For interpretation of the references to color in this figure legend, the reader is referred to the web version of this article.)

The MAOS consists of a two-dimensional automatic goniometer, a spectrometer (QE Pro) and a laptop for control. It automatically collects the canopy radiance at different viewing angles, together with the downwelling solar irradiance reflected from a reference panel. In this study, the multi-angular spectral measurements were taken in the solar principal planes with the view zenith angles ranging from −60° to 60° with an interval of 10° (a smaller interval of 2° was set around the hotspot position). The multi-angular measurements of canopy reflectance and SIF were carried out under stable sunny weather conditions from 8:00 to 16:30 (local time) during eight days of different winter wheat growth stages in 2015 and 2016 (as listed in Table 4). It takes about 7 min for each set of multi-angular measurements. In total, 32 sets of valid measurements were acquired.

Table 4
Parameters of multi-angular measurements on winter wheat at Xiao Tangshan Farm, Beijing, China during the springs of 2015 and 2016.

Date	LAI	Cab (μg/cm^2)	SZA (°)
Apr. 3, 2015	1.46	47.9	43.6–54.5
Apr. 13, 2015	1.94	51.5	38.4–57.8
Apr. 24, 2015	2.40	50.0	32.3–47.4
Apr. 25, 2015	2.40	50.0	31.1–62.4
Apr. 18, 2016	2.92	47.5	36.4–61.5
May 3, 2016	1.93	49.3	29.3–50.5
May 4, 2016	1.93	49.3	32.8–60.5
May 17, 2016	1.43	45.6	27.4–47.6

2.2.3. SIF retrieval

At the canopy level, measured radiance signals comprise the sum of emitted SIF and reflected solar radiation. Disentangling both components is frequently based on the Fraunhofer Line Discrimination (FLD) principle (Plascyk, 1975). Frequently used algorithms include the 3-band FLD (3FLD) (Maier et al., 2003), the improved FLD (iFLD) (Alonso et al., 2008) and the spectral fitting methods (SFM) (Meroni et al., 2010). According to the analysis by Damm et al. (2011), L. Liu et al. (2015) and X. Liu et al. (2015), the 3FLD algorithm is relatively simple and robust for the spectral resolution and SNR of the spectral data acquired by our QE Pro spectrometer. Therefore, we estimated SIF at the canopy level with the 3FLD algorithm. The selected wavelengths are 757.92 nm, 760.72 nm and 768.87 nm for the O2-A band, and 686.44 nm, 687.09 nm and 688.23 nm for O2-B band (Du et al., 2017).

2.2.4. Estimation of $APAR_{chl}$

According to Eq. (2), SIF emission at photosystem level is closely related to APAR (more specifically, PAR absorbed by chlorophyll ($APAR_{chl}$)). $APAR_{chl}$ is difficult to measure directly, but is closely related to the photosynthetically active radiation absorbed by green leaves ($APAR_{green}$) (Du et al., 2017; Porcar-Castell et al., 2014). Liu et al. (2013) proposed an efficient method for making in-situ measurements of the fraction of $APAR_{green}$ ($fAPAR_{green}$) for a low vegetation canopy using a digital camera and a reference panel. A color image of the canopy with the reference panel is first taken by a digital camera at nadir position. Pixels in the image are then classified into green leaves, ground litter, sunlit soil, shaded soil, and reference panel.

Table 3
Parameters of multi-species measurements. Cab stands for leaf chlorophyll $a + b$ content, LIDF is the leaf inclination distribution function, and Fc is the fraction of vegetation coverage.

Site	Location	Date	Species	Cab (μg/cm^2)	LIDF	Fc
Xiao Tangshan (XTS)	40°11′N 116°27′E	Apr. 8, 9 & 18, Nov. 7, Dec. 8, 2016	Winter wheat	21.22–55.29	Spherical	0.15–0.79
Nanbin Farm (NBF)	18°22′N 109°10′E	Dec. 18, 2016	Vegetables and cotton	15.22–56.68	Planophile	0.28–0.91
Sanya Station (SYS)	18°18′N 109°18′E	Dec. 18, 2016	Gold coin grass	40.83	Planophile	0.67

Consequently, the $fAPAR_{green}$ could be calculated as:

$$fAPAR_{green} = \frac{PAR_i - PAR_r - (APAR_{EB} + APAR_{CB})}{PAR_i} \quad (3)$$

where PAR_i and PAR_r are, respectively, the incident and reflected (including all exposed components) PAR derived from the DN values of the digital image. $APAR_{EB}$ and $APAR_{CB}$ are the PAR absorbed by the exposed background (EB, including the non-photosynthetic components) and the vegetation-covered background (CB) respectively.

In the multi-species experiments described in Section 2.2.1, $fAPAR_{green}$ was measured with the digital camera based approach as described above. Unfortunately, $fAPAR_{green}$ was not measured in the multi-angular experiments (Section 2.2.2). To eliminate the saturation effect of the normalized difference vegetation index (NDVI), Gitelson et al. (2014) proposed a wide dynamic range vegetation index (WDRVI), which has been proved to be well linearly correlated with $fAPAR_{green}$ (Viña and Gitelson, 2005). The WDRVI is defined as:

$$WDRVI = (\alpha R_{NIR} - R_{Red})/(\alpha R_{NIR} + R_{Red}) \quad (4)$$

where R_{NIR} and R_{Red} are the reflectances at the near infrared and red band, respectively, and α is a weighting coefficient with a value of 0.1–0.2 (Gitelson et al., 2014). Fig. 2 shows the relationship between WDRVI (α = 0.1) and $fAPAR_{green}$ for SCOPE simulations with different values of the LAI (1–4), leaf chlorophyll content (20–80 μg/cm^2), SZA (20–60°) and three typical leaf inclination distribution functions (planophile, plagiophile and spherical). Therefore, in the multi-angular experiments $fAPAR_{green}$ was estimated using the linear model based on the WDRVI.

Chlorophyll is the main absorbing compound for PAR in green leaves (Jacquemoud and Baret, 1990; Porcar-Castell et al., 2014). According to Du et al. (2017), $fAPAR_{chl}$ can be approximated from $fAPAR_{green}$ with a linear function:

$$fAPAR_{chl} = k \times fAPAR_{green} \quad (5)$$

where the coefficient k is related to the leaf chlorophyll content. Analysis of SCOPE simulations conducted by Du et al. (2017) revealed that the value of k varies from 0.78 to 0.80 for the leaf chlorophyll content from 20 to 60 μg/cm^2. Since the leaf chlorophyll content of most of the samples was within the range 20–60 μg/cm^2 (except for one sample for which the value was 15.22 μg/cm^2), we estimated $fAPAR_{chl}$ using k equal to 0.79 in this study.

The incident photosynthetically active radiation (PAR) was calculated using the radiance reflected from a white reference panel measured by a spectrometer. Consequently, the $APAR_{chl}$ can be calculated as:

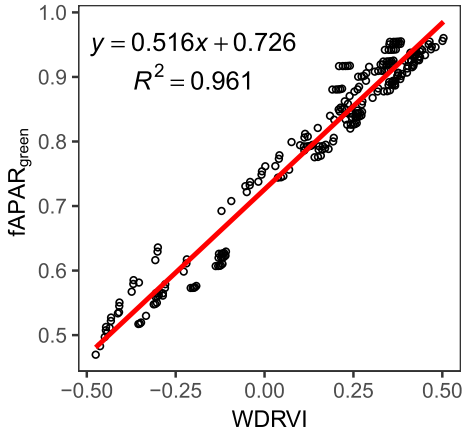

Fig. 2. Linear regression of the fraction of photosynthetically active radiation absorbed by green leaves ($fAPAR_{green}$) on the wide dynamic range vegetation index (WDRVI) computed from SCOPE simulations for canopies with different leaf area indices, leaf chlorophyll contents and leaf inclination distributions.

$$APAR_{chl} = PAR \times fAPAR_{chl} \quad (6)$$

2.3. Airborne measurements

The airborne image, used to evaluate the method introduced in this study, was acquired using the imaging spectrometer *HyPlant* (Specim, Oulo, Finland). As an airborne demonstrator for the ESA's Fluorescence Explorer (FLEX) mission, *HyPlant* was specifically designed for the monitoring of vegetation canopy spectral characteristic parameters, including SIF. There are two modules in *HyPlant:* the first is the FLUO module, which is used for the SIF measurements and which covers the range from 670 nm to 780 nm with a high spectral resolution (FWHM = 0.25 nm); the other module is the DUAL module, which covers a broader spectral range (380–2500 nm) with a FWHM of ~4 nm for bands from 380 nm to 970 nm, and of ~13.3 nm for bands from 970 nm to 2500 nm. More technical details about the *HyPlant* configurations and the data processing are available in Rascher et al. (2015).

In this study, we used a *HyPlant* image acquired at 14:58 (local time) on June 30, 2015 over the study area located in the Ruhr catchment in the central western part of North Rhine-Westphalia, Germany (50.864° N, 6.452° E). The flight height of 600 m above ground and the swath wide of ~400 m resulted in a spatial resolution of 1 m and view zenith angles from 0° to about 16.7° from the center to the edges of the swath. The flight heading direction was 345.89°, under the solar zenith angle of 31.89°, and the solar azimuth angle of 217.52°.

The far-red (760 nm) and red (687 nm) SIF at canopy level were retrieved using the iFLD method (Alonso et al., 2008). A semi-empirical technique that made use of SIF-free reference pixels (e.g., bare soil) was used to empirically account for uncertainties in estimated upward transmittance of the atmosphere (Damm et al., 2014). For further technical details of SIF retrieval from the *HyPlant* image, please refer to Damm et al. (2014) and Wieneke et al. (2016). $fAPAR_{green}$ was estimated using the WDRVI-based linear model that was introduced in Section 2.2.4. As explained in Section 2.2.4, the linear relationship between $fAPAR_{chl}$ and $fAPAR_{green}$ was assumed also for the *HyPlant* image. The missing of information about chlorophyll content made it difficult to decide a proper coefficient for the $fAPAR_{chl}$ - $fAPAR_{green}$ relationship, so we did not calculate the $fAPAR_{chl}$ for the *HyPlant* image, but used the $fAPAR_{green}$ directly to evaluate the results of SIF downscaling.

2.4. Physical analysis of SIF radiation transfer within the canopy

The absorption and scattering of SIF photons within the canopy is ruled by the same physical interactions as in the case of the reflected radiation. The difference is only the location of the photons' source. SIF photons are emitted inside the leaves while, photons of reflected radiation originate from the solar illumination at the top of canopy (Fig. 3).

Using the concept of recollision probability (so-called '*p*-theory') (Stenberg et al., 2016) and assuming that the canopy is bounded underneath by a non-reflecting surface (the 'black-soil' condition), the four probable states of photons originating from solar illumination are as illustrated in Fig. 3(a) (Smolander and Stenberg, 2005). The canopy absorptance can be expressed as:

$$a_i(\lambda) = i_0[(1 - \omega_L(\lambda)) + \omega_L(\lambda)p(1 - \omega_L(\lambda)) + \omega_L(\lambda)^2p^2(1 - \omega_L(\lambda)) + \ldots] = i_0\frac{1 - \omega_L(\lambda)}{1 - p\omega_L(\lambda)} \quad (7)$$

where p is the recollision probability, ω_L is the leaf scattering coefficient (single scattering albedo), and i_0 is the canopy interceptance of the incoming radiation. The canopy scattering can then be expressed as:

$$s_i(\lambda) = i_0 - a_i(\lambda) = \frac{1 - p}{1 - p\omega_L(\lambda)}i_0\omega_L(\lambda) \quad (8)$$

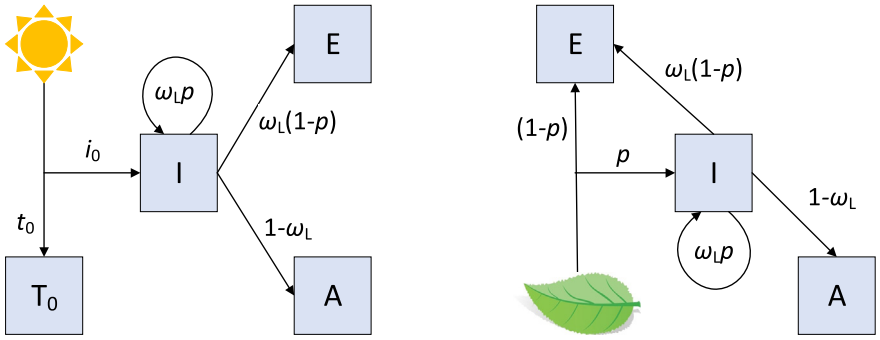

Fig. 3. An illustration of the canopy absorption and scattering model for solar illumination (a) and SIF emission (b) assuming with non-reflecting soil background. State T_0 represents photons that go through the canopy without interacting with the canopy or being absorbed by the soil; state I represents photons that interact with the canopy; state A represents photons absorbed by the canopy; and state E represents photons that escape from the canopy. p is the recollision probability, ω_L is the leaf scattering coefficient (single scattering albedo), i_0 is the canopy interceptance of the incoming radiation, which means the probability of an incident photon that will be intercepted by the canopy, and t_0 is the probability that a photon can pass through the canopy without any interactions ($t_0 = 1 - i_0$).

The recollision probability describes the multiple scattering process within the canopy. To describe the anisotropic escape probability of photons to leave the canopy, the bi-directional gap fraction, another spectral invariant, is needed. The term $(1 - p)$ can be expressed as the integrated canopy density over all directions in the unit sphere (Knyazikhin et al., 2013):

$$1 - p = \frac{1}{\pi}\int_{4\pi} \rho(\Omega)|\mu|\, d\Omega \tag{9}$$

where $\rho(\Omega)$ is the gap fraction for direction Ω, 4π denotes the unit sphere, and μ is the cosine of the polar angle of Ω. The canopy structure is the main factor influencing its reflectance anisotropy. According to Knyazikhin et al. (2011, 2013), the bi-directional reflectance factor (BRF), representing the canopy scattering in a specific observing direction, can be approximately expressed as:

$$\mathrm{BRF}(\lambda, \Omega_s, \Omega_v) = \frac{\rho(\Omega_s, \Omega_v)}{1 - p\omega_L(\lambda)} i_0 \omega_L(\lambda) \tag{10}$$

where $\rho(\Omega_s, \Omega_v)$ is the bi-directional gap fraction which contains the information of canopy structure and the fraction of sunlit and shaded leaves. Ω_s and Ω_v are the solar and view directions, respectively.

Similarly, for SIF emission, the probable states of the SIF photons emitted from leaves are as illustrated in Fig. 3(b). It needs to be noted that, there is also probability for SIF photons to be absorbed by the soil without any interactions in the canopy (similar as the state of T_0 in Fig. 3(a)). However, such probability is considered to be very low, because the SIF photons absorbed by soil directly are most likely from the bottom leaves, while the illumination on leaves at the bottom of canopy is usually very low for dense canopy. Additionally, for the red-band, the downward SIF at leaf level has been proved to be much weaker than the upward SIF (Van Wittenberghe et al., 2015). Therefore, the portion of SIF photons directly absorbed by the soil is neglected in this study. Accordingly, the canopy absorptance of SIF photons can be expressed as:

$$a_f(\lambda) = p(1 - \omega_L(\lambda)) + \omega_L(\lambda)p^2(1 - \omega_L(\lambda)) + \omega_L(\lambda)^2 p^3(1 - \omega_L(\lambda)) + \ldots = p\frac{1 - \omega_L(\lambda)}{1 - p\omega_L(\lambda)} \tag{11}$$

and the canopy scattering of SIF photons as:

$$s_f(\lambda) = 1 - \mathrm{a}_f(\lambda) = \frac{1 - \mathrm{p}}{1 - p\omega_L(\lambda)} \tag{12}$$

The scattering processes for SIF photons and for reflected photons by canopy elements are similar. Consequently, the SIF escape probability from leaf level to canopy level ($\varepsilon_{CL} = SIF_{Canopy}/SIF_{Leaves}$) in observing direction Ω can be expressed as:

$$\varepsilon_{CL}(\lambda, \Omega) = \frac{\rho(\Omega)}{1 - p\omega_L(\lambda)} \tag{13}$$

If we substitute Eq. (10) into Eq. (13), then we have,

$$\varepsilon_{CL}(\lambda, \Omega) = \frac{\mathrm{BRF}(\lambda, \Omega)}{i_0 \omega_L(\lambda)} \tag{14}$$

According to the analysis above, under the 'black-soil' condition, the SIF escape probability from leaf to canopy level is related to the directional reflectance, the canopy interceptance and the leaf scattering coefficient. In practice, the directional reflectance can be acquired concurrently with the SIF measurements, but canopy interceptance and leaf scattering coefficients cannot, in general, be accurately estimated. The canopy interceptance is driven by the canopy structure and the actual solar position. If the clumping effect is assumed to be of minor impact, the canopy interceptance can be expressed as (Chen and Black, 1992; Ross, 2012):

$$i_0 = 1 - \exp\left(\frac{-G(\theta) \bullet LAI}{\cos(\theta)}\right) \tag{15}$$

where θ is the SZA and $G(\theta)$ is the mean projection coefficient for foliages on a plane perpendicular to θ. The function, G, is determined by the LIDF. For the spherical leaf inclination distribution type with an LIDF that is a sine function, the value of G is 0.5 and is independent of θ. For other values of the LIDF, the value of G ranges from 0 to 1 when θ varies from 0° to 90°, and generally converges to 0.5 when θ is approximately 57.3° for all LIDF types (Nilson, 1971; Ross, 2012; Ryu et al., 2010). $G(\theta) \cdot LAI$ represents the projected LAI in the solar direction.

Fig. 4 shows the values of i_0 for different values of G, LAI and SZA. For a dense canopy with large values of LAI and G, the value of i_0 is close to 1, while for sparse canopies, the value of i_0 shows a large degree of variability.

Since absorption by chlorophyll a molecules is very weak at the far-red band, leaf single scattering albedo (ω_L) is strongly influenced by chlorophyll content only in the red wavelengths of SIF emission. $\omega_L$at the far-red band is, therefore, almost independent of chlorophyll content and it is driven by a minor absorptance of leaf tissue biochemical compounds. Fig. 5 shows the variations of ω_L at the far-red (760 nm) and red (687 nm) bands simulated by the Fluspect model for leaf chlorophyll content from 10 to 80 μg/cm^2. As expected, the value of ω_L at the far-red band is almost invariant, reaching values between 0.853 and 0.888, while it varies from 0.044 to 0.287 for the red band, where the absorption by chlorophyll is strong. It exhibits a large variation in the value of ω_L, especially for the chlorophyll content lower than 40 μg/cm^2.

Another fact needs to be noted is, the spectral invariant theory ignores the difference between the leaf reflectance and leaf transmittance (combined as ω_L). Therefore, the spectral invariant theory performs well at the far-red band, where multi-scattering dominates, but not so well at the red band, where single scattering dominates. Nevertheless, the ε_{CL} and $\frac{\mathrm{BRF}}{i_0\omega_L}$ are still proportional at the red band (Yang and Van der Tol, 2018). This problem is discussed in Section 4.4.

The escape probability for SIF from the PS level to the leaf level

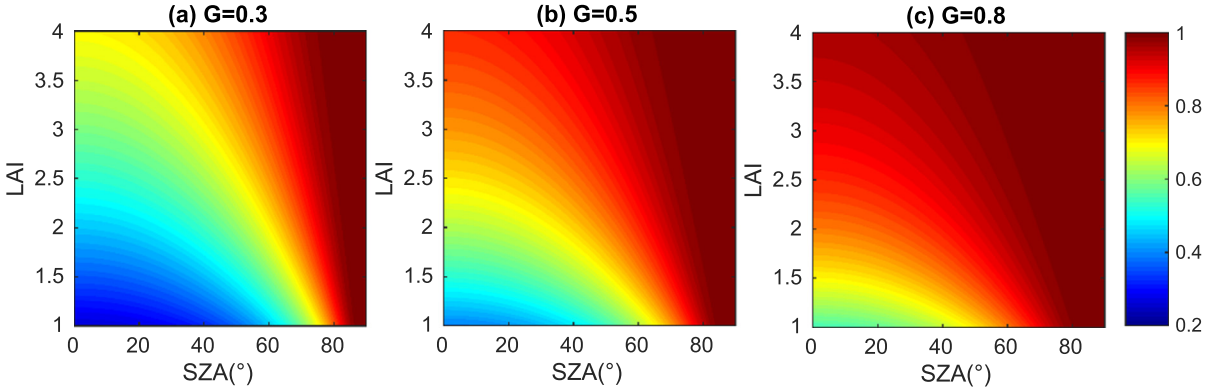

Fig. 4. Values of the canopy interceptance of the incoming radiation (i_0) for different G function values, leaf area index (LAI) and solar zenith angle (SZA) combinations, calculated using Eq. (15). G function is the mean projection coefficient for foliages on a plane perpendicular to the solar zenith direction.

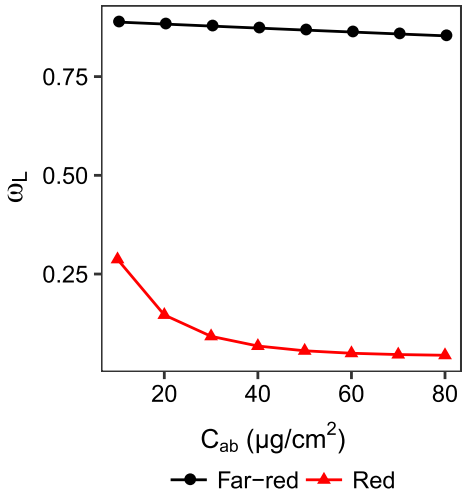

Fig. 5. Values of ω_L at the far-red (760 nm) and red (687 nm) bands simulated by the Fluspect model for different values of the leaf chlorophyll content. The values for other input parameters for the Fluspect model were set as default (same as in Table 1). (For interpretation of the references to color in this figure legend, the reader is referred to the web version of this article.)

(ε_{LP} = SIF_{Leaves}/SIF_{PS}) is related to the leaf internal absorptance (from the photosystems to the leaf surface). The leaf internal absorptance at the spectral range of the SIF emission is caused mainly by the leaf chlorophyll content, but the relationship is non-linear, because the increment in radiation absorption per unit of chlorophyll decreases at high chlorophyll content (Adams et al., 1990; Gitelson et al., 1998; Porcar-Castell et al., 2014). Besides, chlorophyll molecules are distributed in different cell layers of leaf mesophyll tissues. Although the radiative transfer processes at the molecular-level are complex for accurate modelling, ε_{LP} can be expressed as a non-linear function of the chlorophyll content (Cab) and wavelength as:

$$\varepsilon_{LP}(\lambda) \approx f(\mathrm{Cab}, \lambda) \tag{16}$$

Consequently, the SIF escape probability from the PS level to the canopy level (ε_{CP}) can be expressed as:

$$\varepsilon_{CP}(\lambda, \Omega) = \varepsilon_{LP}(\lambda) \bullet \varepsilon_{CL}(\lambda) \approx f(\mathrm{Cab}, \lambda) \bullet \frac{\mathrm{BRF}(\lambda, \Omega)}{i_0 \omega_L(\lambda)} \tag{17}$$

To summarize, the SIF escape probability from the PS level to the canopy level can be approximately modeled using the canopy BRF, canopy interceptance and Cab, under the assumption of 'black-soil' condition. For remote sensing observations, the directional reflectance is available. However, the i_0 and ω_L is not easy to be accurately measured or estimated. According to Eq. (15) and Fig. 4, i_0 is related to canopy structure, which is not easy to be accurately retrieved with optical remote sensing approaches. It is not possible to observe leaf reflectance and transmittance directly at canopy level, and ω_L varies among different leaves. So ω_L is also difficult to be estimated from remote sensing observations at canopy level. But for a dense canopy and for leaves with a relatively high value of Cab, i_0 and ω_L are relatively stable, and the directional reflectance is the main factor that influences ε_{CP}, especially at the far-red band.

2.5. Estimation of ε_{CP} and ε_{CL} using the random forest approach

Given the difficulties involved in acquiring the parameters required for physical modelling of the SIF downscaling, a statistical model based on the Random Forest (RF) regression, which is one of the most effective machine learning models for predictive analytical approaches (Breiman, 2001), was trained on the dataset simulated in SCOPE to estimate ε_{CP}.

As shown in Section 2.4, the BRF has significant impact on ε_{CP}. Taking all other factors together as f_{CP}, Eq. (17) can be modified thus:

$$\varepsilon_{CP}(\lambda, \Omega) = f_{CP} \bullet \mathrm{BRF}(\lambda, \Omega) \tag{18}$$

where f_{CP} is the ratio of ε_{CP} to BRF. In the SCOPE simulations, $\varepsilon_{CP}(\lambda, \Omega)$ and $\mathrm{BRF}(\lambda, \Omega)$ can be simulated directly, and f_{CP} later calculated. As f_{CP} is acquired from SCOPE simulation instead of physical analysis, the assumption of 'black-soil' condition for Eq. (17) is no longer needed here. Similarly, ε_{CL} can be expressed as,

$$\varepsilon_{CL}(\lambda, \Omega) = f_{CL} \bullet \mathrm{BRF}(\lambda, \Omega) \tag{19}$$

We only estimated f_{CP} or f_{CL} with the random forest approach to increase robustness of estimated ε_{CP} and ε_{CL}. Directional reflectance was obtained from measurements or simulations. f_{CP} and f_{CL} are mainly related to the leaf scattering coefficient and canopy structure. These kinds of information can be derived from directional reflectance at different bands and from various vegetation indices.

At the near infrared band, the canopy reflectance is dominated by the scattering effect, which primarily originates from the leaf and canopy structure. At the red band, the canopy reflectance is dominated by the absorption effect of chlorophyll pigments (Colwell, 1974; Sims and Gamon, 2002). It has been demonstrated that the red-edge band is important for the estimation of Cab as it is less impacted by the absorption saturation effect for a high Cab than the red band (Clevers and Gitelson, 2013; Dash and Curran, 2004; Gitelson et al., 2005; Malenovský et al., 2013). Several vegetation indices (VIs), based on the reflectance at the red, red-edge and near infrared bands, have been developed for the retrieval of vegetation parameters. In this study, the NDVI, simple ratio (SR) and the MERIS terrestrial chlorophyll index (MTCI) were used (formulae and references in Table 5). Considering the possible available wavelength range of spectral measurements for SIF

Table 5
Mathematical formulations and references for the Vis (R_{758}, R_{685} and R_{710} stand for the directional reflectance at 758 nm, 685 nm and 710 nm, respectively).

Equation	Reference
$NDVI = (R_{758} - R_{685}) / (R_{758} + R_{685})$	(Rouse et al., 1973)
$SR = R_{758} / R_{685}$	(Jordan, 1969)
$MTCI = (R_{758} - R_{710}) / (R_{710} - R_{685})$	(Dash and Curran, 2004)

retrieval, and to avoid the SIF in-filling effect at the oxygen absorption bands at about 687 nm and 760 nm, we selected 685 nm as the red band, 710 nm as the red-edge band, and 758 nm as the near infrared band for the calculation of the VIs. The NDVI is sensitive to the canopy structural parameters such as LAI (Soudani et al., 2012). The SR is sensitive to the chlorophyll absorption at the red band. Finally, MTCI was designed for estimation of the chlorophyll content (Dash and Curran, 2004). Consequently, NDVI, SR and MTCI, together with the canopy directional reflectance at 685 nm, 710 nm and 758 nm, were selected as the potential input variables to establish the RF regression. The scatter matrix of the relationships among the potential input variables and f_{CP} is provided in the Supplementary materials (Fig. S1). The final selection of inputs was decided by testing the performance of RF regression with different combinations of the six potential variables, which is shown in Section 3.1.

500 decision trees were used to construct the RF model, and the minimum number of terminal nodes were set as 5. The SCOPE simulations (cf., Section 2.1.1), which cover most common vegetation conditions, were employed for the training of the RF. SIF of the red (687 nm) and far-red (760 nm) bands at canopy, leaf, and PS levels were simulated by the SCOPE model, together with the directional reflectance at 685 nm, 710 nm and 758 nm. Consequently, f_{CP} and f_{CL} could be calculated according to Eqs. (18) and (19), respectively.

3. Results

3.1. Selection of the inputs for the RF regression

To optimize the inputs for the RF regression, we tested the performance of the RF model with different combinations of the six potential input parameters explained in Section 2.5. Firstly, all the six potential parameters were used as the inputs for the RF regression to calculate their relative importance using the mean decrease accuracy (MDA) method based on the concept of out-of-bag (OOB) error. The OOB error is a parameter that represents the RF prediction error. It is considered as the mean prediction error on each training sample x_i, which uses only the trees that did not have x_i in their bootstrap sample (Breiman, 2001). To measure the importance of the j-th feature for training, the values of the j-th feature are permuted among the training data and the OOB error is computed for each perturbed data set. The importance score for the j-th feature is computed by averaging the difference in the OOB error before and after the permutation over all trees. Fig. 6 shows the relative importance of the input variables of the RF model for SIF downscaling from canopy level to leaf level or PS level. These results indicate that the far-red directional reflectance and MTCI were found as the most important variables for the SIF downscaling model at both the far-red and red bands, while the importance of the directional reflectance at the red and red-edge bands, the NDVI, and the SR was on similar, lower level.

Secondly, the performance of the RF model was tested with different combinations of input parameters. 2/3 of the SCOPE simulations were randomly selected to train the RF model, and the remaining 1/3 were used as reference samples to evaluate the performance of the trained model with the relative root-mean-square error with respect to mean value (RRMSE) and the coefficient of determination (R^2). To reduce the random errors, for each combination of input parameters, 30 RF models

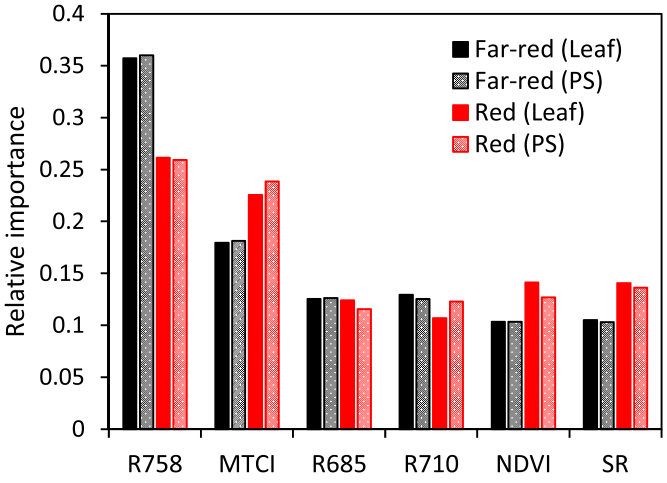

Fig. 6. Relative importance of input variables of the RF model for SIF downscaling from canopy level to leaf level or PS level. R_{758}, R_{685} and R_{710} stand for the directional reflectance at 758 nm, 685 nm and 710 nm, respectively.

were trained and the RRMSE and R^2 were averaged. The results are listed in Table 6. In addition, a significance test was also carried out for further comparing the performance of different combinations of input parameters (shown in Table S1). For the far-red band, when four parameters (R_{758}, MTCI, R_{685}, R_{710}) were used, the RRMSE and R^2 became relatively stable, and the difference comparing with using all six parameters became insignificant (the p-value is 0.273 and 0.335 for leaf level and PS level, respectively). When adding more input parameters (SR and NDVI), the variation of RRMSE was $< 0.5\%$. For the red band, in contrast, the difference between the performance of using four input parameters (R_{758}, MTCI, R_{685}, R_{710}) and using all six parameters was still significant for both leaf level and PS level (p-value $< 10^{-9}$, see Table S1). When adding SR or NDVI as the input parameters, the RRMSE of the RF model was improved clearly (the RRMSE was reduced about 10% for the leaf level and about 6% for the PS level). But the performance of the RF model had no significant improvement when using both SR and NDVI (p-values > 0.300, see Table S1). The results also indicated that, although the vegetation indices can be calculated using the reflectance at the three wavelengths, they can still provide important information for the estimation of f_{CL} and f_{CP}, because vegetation indices are able to enhance some information by non-linearly combining the reflectance at different wavelengths, and the special non-linear relationship may be difficult for the RF regression to find out.

According to the results, R_{758}, MTCI, R_{685}, and R_{710} were selected as the input parameters of the RF model for the estimation of f_{CL} and f_{CP} at the far-red band, while R_{758}, MTCI, R_{685}, R_{710}, and SR were selected for the red band.

3.2. Evaluation of the SIF downscaling accuracy using SCOPE and DART simulations

SCOPE and DART based simulations were used in the first instance to quantitatively evaluate the performance of the RF approach for SIF downscaling. SCOPE allows simulating SIF values at the canopy, leaf, and PS levels, but there is no module for SIF simulation at PS level in DART, so the DART model is only able to provide the SIF values at the canopy and leaf levels.

The SCOPE simulations were first used for accuracy assessments at the leaf and PS levels. 2/3 of the SCOPE simulations were randomly selected to train the RF model, and the remaining 1/3 was used for validation. Fig. 7 shows a comparison of the far-red and red SIF estimated by the RF approach with the reference SIF simulated by SCOPE for the leaf and PS levels. In general, the estimated values of SIF at the

Table 6
The relative root-mean-square error (RRMSE) and the coefficient of determination (R^2) of RF models for the ratios of SIF escape probability to BRF (f_{CL} for leaf level to canopy level and f_{CP} for photosystem level to canopy level) at far-red and red bands with different combinations of input parameters.

Input parameters	f_{CL} (Far-red)		f_{CP} (Far-red)		f_{CL}(Red)		f_{CP} (Red)	
	RRMSE	R^2	RRMSE	R^2	RRMSE	R^2	RRMSE	R^2
R_{758}, R_{710}, R_{685}	0.0492	0.871	0.0569	0.901	0.0981	0.960	0.0942	0.954
R_{758}, MTCI, R_{685}	0.0463	0.886	0.0502	0.928	0.0990	0.961	0.0969	0.957
R_{758}, MTCI, R_{685}, R_{710}	0.0462	0.886	0.0489	0.931	0.0871	0.964	0.0849	0.961
R_{758}, MTCI, R_{685}, R_{710}, SR	0.0461	0.887	0.0487	0.931	0.0804	0.968	0.0797	0.964
R_{758}, MTCI, R_{685}, R_{710}, NDVI	0.0463	0.886	0.0488	0.930	0.0800	0.969	0.0797	0.964
R_{758}, MTCI, R_{685}, R_{710}, SR, NDVI	0.0461	0.887	0.0487	0.931	0.0799	0.969	0.0795	0.966

leaf and PS levels matched well with the reference values. Most of the points were located near to the 1:1 line, and the values of the coefficient of determination (R^2) were higher or close to 0.9. The estimation of red SIF at the PS level was not as robust as that of the far-red SIF, but the root-mean-square error (RMSE) was still as low as 3.613 mW/m^2/nm, resulting in the relative root-mean-square error (RRMSE) of 7.299%. The relationship of SIF at canopy level and leaf level, SIF at leaf level and PS level, SIF at canopy level and PS level from SCOPE simulations are also provided in the Supplementary materials (Fig. S2) for comparisons.

Simulations performed in the 3-D DART model (cf., Section 2.1.2) were used for further evaluation of the RF model trained by the SCOPE simulations. Since DART produced canopy and leaf SIF simulations for two modeled canopies of maize and spruce, only the downscaling of SIF from the canopy level to the leaf level could be evaluated. Fig. 8 shows SIF simulated by DART at canopy and leaf level vs. estimates of downscaled SIF. The leaf SIF estimates for the maize canopy were more robust (less variable) for the spruce canopy, but the downscaled estimates matched well the reference values in both cases. The RRMSE between the estimated and reference far-red and red leaf SIF was 7.42% and 12.10% for the maize canopy, and 7.57% and 25.92% for the spruce canopy.

The evaluation carried out on datasets simulated by two different radiative transfer models using different vegetation representations and solar-viewing geometries revealed accurate and robust performance of the RF downscaling approach, especially for the far-red SIF. The lower

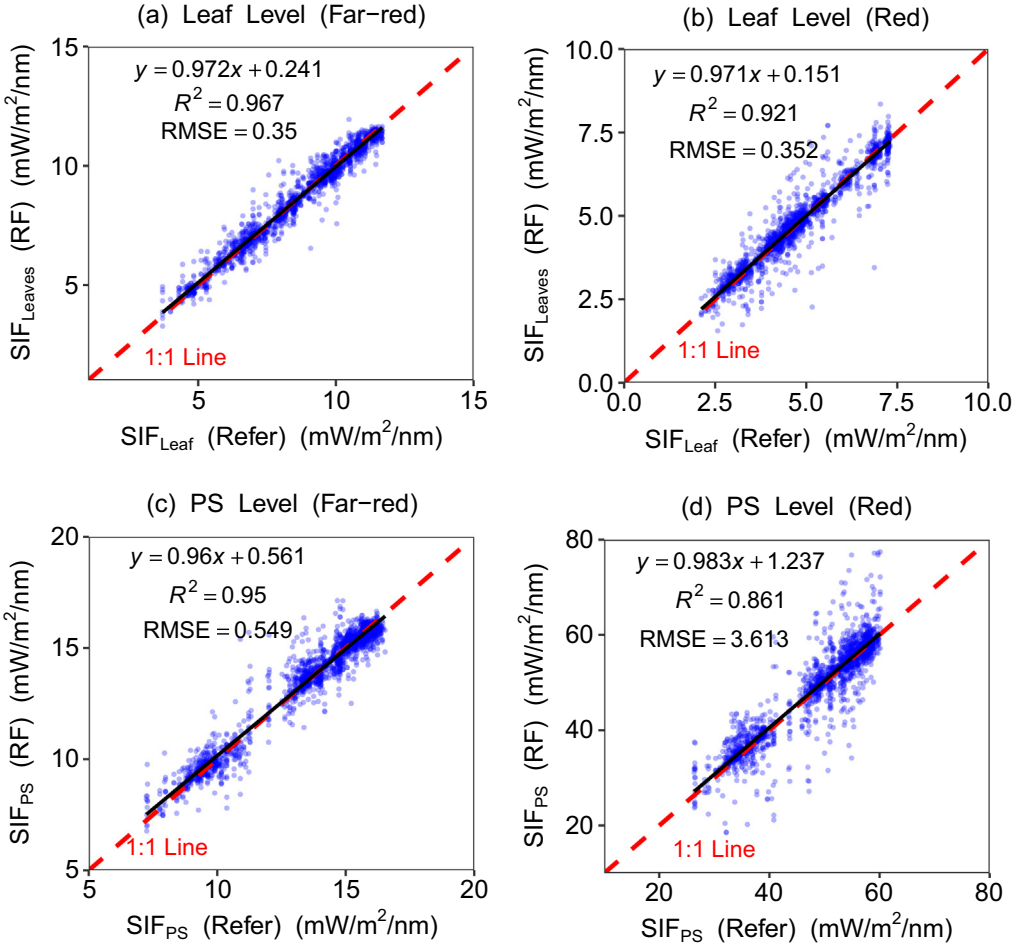

Fig. 7. Comparison of far-red (760 nm) and red (687 nm) SIF estimated by the RF approach with reference SIF simulated by SCOPE for leaf and PS levels. R^2 is the coefficient of determination, and RMSE is the root-mean-square error. (For interpretation of the references to color in this figure legend, the reader is referred to the web version of this article.)

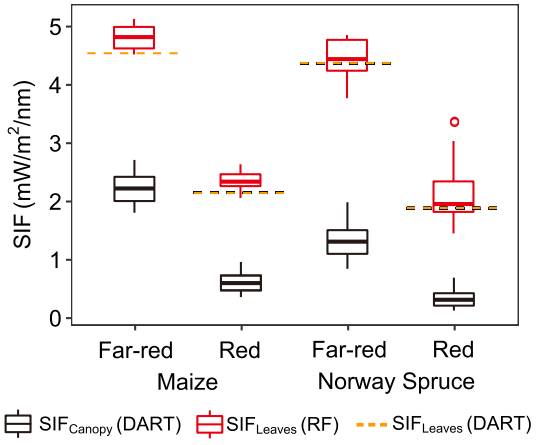

Fig. 8. Boxplot of far-red (740 nm) and red (687 nm) SIF simulated by DART for maize and spruce canopies and corresponding downscaled leaf SIF using the Random Forest (RF) model. The orange dashed line shows the reference values of SIF at leaf level, as simulated in DART by Fluspect. The bottom and top of each box represent the first and third quartiles, respectively, the thick horizontal line in the box is the median, the whiskers show the maximum/minimum values within 1.5 times the interquartile range (IQR, the difference between the third and the first quartiles), and the circles show the outliers out of 1.5IQR. The units of $mW/m^2/nm/sr$ were applied to SIF at canopy level as well as leaf level to make the values comparable. (For interpretation of the references to color in this figure legend, the reader is referred to the web version of this article.)

accuracy for the red band is discussed in Section 4.4.

3.3. Evaluation of SIF downscaling through in-situ multi-species experiments

Under conditions with no stress and with high light, the SIF yield varies little (Van der Tol et al., 2014; Damm et al., 2015a), so the total SIF emission of a plant at PS level is strongly related to $APAR_{chl}$. However, SIF at the canopy level is strongly influenced by re-absorption and scattering effects, which are related to leaf pigments and the canopy structure. Therefore, we compared $APAR_{chl}$ measured for multi-species canopies of different structures with SIF downscaled to PS level with the RF approach (cf., Section 2.2.1).

Fig. 9 shows the relationship between $APAR_{chl}$ and nadir-observed canopy SIF, SIF at leaf level and SIF at PS level estimated by the RF approach. The relationship between $APAR_{chl}$ and SIF_{Canopy} varied for different species, while the slope of the linear regression lines of the SIF-$APAR_{chl}$ models for different species became closer to each other when SIF was downscaled from canopy level to PS level, which indicated that the relationship between $APAR_{chl}$ and SIF_{PS} was less species-dependent. At the far-red band, the values of R^2 increased significantly when SIF was downscaled from canopy level to leaf level, but did not vary much (decreased a little) when SIF was further downscaled to the PS level. Differently, at the red band, the R^2 for the PS level was much higher than that for the leaf level.

The linear regression models of the SIF-$APAR_{chl}$ relationship for different species at canopy, leaf and PS levels were summarized in Table 7, and the coefficients of variation (CV) of the slopes for different species at each level were also calculated. For grass and wheat, the relationships between SIF at all levels and APAR were close to linear. But for the vegetation, the relationship was some erratic, especially at the red band. The reason may partly due to the measurement errors. For both the far-red and red bands, the CV of slopes for different species decreased significantly when SIF was downscaled from canopy level to leaf or PS level. At the far-red band, both the CV of slopes and the R^2 of each model at the PS level were very close to that at the leaf level. At the red band, the CV of slopes at the PS level was some higher than that for the leaf level, but the R^2 of the regression model for all the three species were higher than that at the leaf level, especially for the model of the vegetables (increased from 0.1964 to 0.4455 when SIF was downscaled from leaf level to PS level).

The results shown in Fig. 9 and Table 7 confirmed that the species-dependency of the SIF-$APAR_{chl}$ relationship could be reduced by SIF downscaling from canopy level to leaf or PS level. These results also indicated that the canopy structure is the main factor influencing the far-red SIF escape probability, while the leaf internal absorption mainly influence the red SIF.

3.4. Evaluation of SIF downscaling using multi-angular experiments

The SIF emission at the PS level can be regarded as isotropic whereas, due to re-absorption and scattering within the canopy, the observed SIF at the canopy level is obviously anisotropic. Consequently, multi-angular measurements of a winter wheat canopy (cf., Section 2.2.2) were used for further evaluation of the SIF downscaling approach, in particular its potential to normalize the anisotropy in the SIF measurements.

Fig. 10 shows the relationship between $APAR_{chl}$ and values of the multi-angular observed SIF at canopy level, leaf level or PS level in the form of boxplots. The $APAR_{chl}$ values were divided into groups with an interval of $5\,W/m^2$. Moreover, for each set of multi-angular observations (with different VZAs in the solar principal plane), we calculated the coefficients of variation (CV) of SIF at canopy level, leaf level or PS level, as shown in Fig. 11. Lower CV values indicated less anisotropy of SIF. The results shown in Figs. 10 and 11 demonstrate that, for each $APAR_{chl}$ level, SIF at canopy level varied substantially at both the far-red and red bands due to its anisotropic characteristics caused by the scattering within the canopy. Computed CV values varied from 0.12 to 0.32 for the far-red band, and from 0.33 to 0.61 for the red band. The value of R^2 for the relationship between SIF_{Canopy} and $APAR_{chl}$ is 0.43 and 0.09 for the far-red band and the red band, respectively. The estimated SIF at the leaf level and PS level was much more closely related to $APAR_{chl}$ and the variation of SIF in predefined $APAR_{chl}$ level was visibly reduced. At the far-red band, the value of R^2 for the relationship between SIF_{PS} and $APAR_{chl}$ was 0.76, and the values of CV for SIF_{PS} varied from 0.04 to 0.18. At the red band, there were some outliers in the boxplot which indicates a less robust performance of the SIF downscaling. Overall, the value of R^2 for the relationship between SIF_{PS} and $APAR_{chl}$ was 0.14, and the values of CV for SIF_{PS} for most sets of multi-angular observations were also reduced and lie within the range 0.14 to 0.42. The results for SIF downscaling to leaf level and to PS level were very similar, because the leaf absorptance did not vary a lot (the chlorophyll contents for all the samples were very similar as shown in Table 4). The results also confirmed the assumption that the SIF emission at both leaf level and PS level is isotropic.

3.5. Downscaling of canopy SIF retrieved from HyPlant image

Besides the ground-based measurements, in this study, a *HyPlant* image was also employed for the evaluation of the SIF downscaling results. Before application of SIF downscaling, the original pixel size of the *HyPlant* was reduced from 1 m × 1 m to 5 m × 5 m in order to reduce the influence of sensor noise.

Next to the true color composite of the *HyPlant* image, Fig. 13 shows $fAPAR_{green}$, canopy SIF retrieved by the iFLD method, and SIF at leaf and PS levels as estimated by the RF approach for both far-red and red bands. In Fig. 12, an obvious variation in the value of ε_{CP} for the different fields can be seen. As an example, *Field A* (witer wheat) and *Field B* (potato) feature similar levels of $fAPAR_{green}$ and SIF_{PS} but their SIF_{Canopy} were quite different, which indicated significant differences in their canopy structure (see the color of *Field A* and *Field B* in the true color image in Fig. 12). Their different relationships between $fAPAR_{green}$ and SIF_{Canopy} could be attributed to the differences in ε_{CP}. Moreover, the *HyPlant* results also demonstrated that the SIF anisotropy

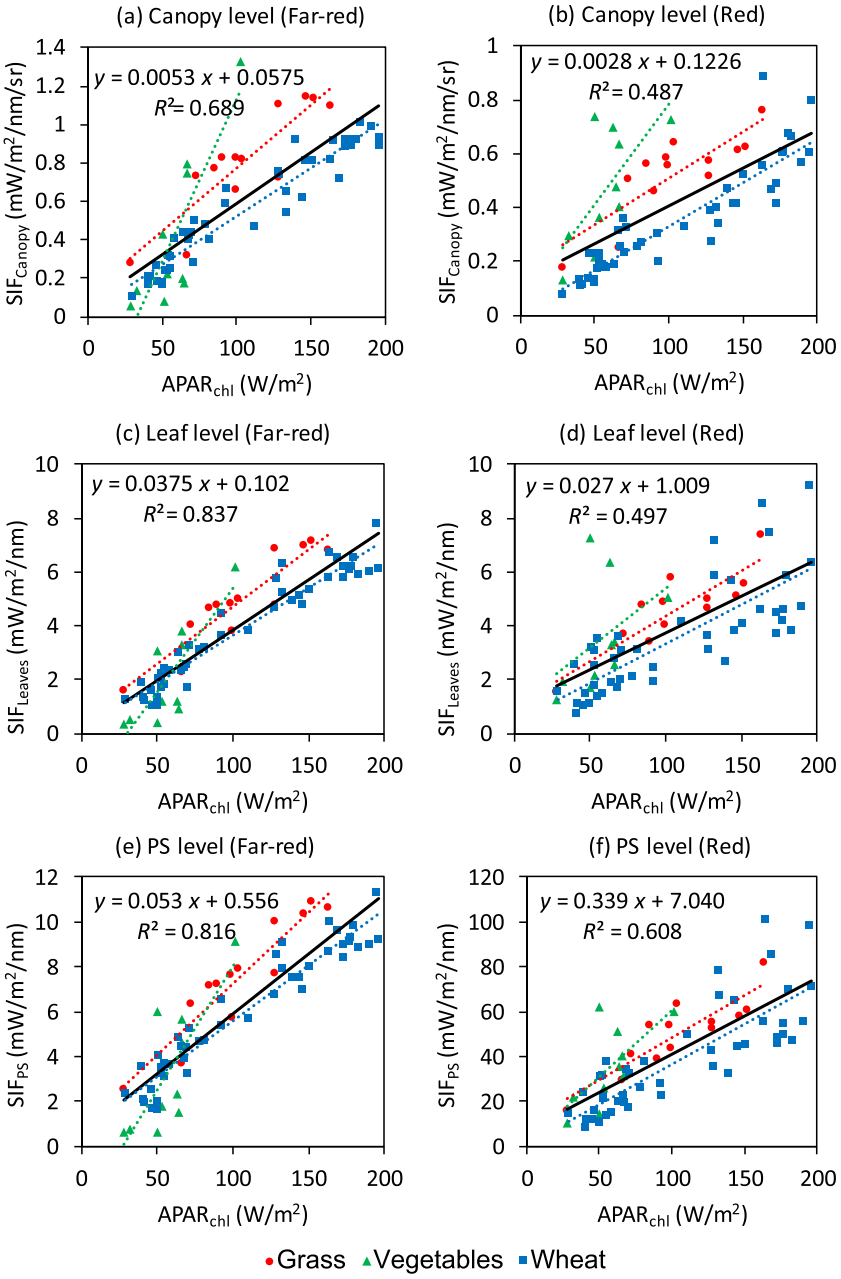

Fig. 9. The relationship between $APAR_{chl}$ and canopy SIF observed at nadir (a, b), SIF at leaf level (c, d) and PS level (e, f) estimated by the RF approach for several different species (grass, various vegetables and wheat). The colored dash lines are the linear regression lines for specific species. The black solid lines and the equations are the linear regression lines and models for all the samples.

Table 7
Linear regression models of the SIF-$APAR_{chl}$ relationship for different species at canopy, leaf and photosystem (PS) levels. The 'CV of slopes' are the coefficients of variation of the slopes for different species at specific levels.

Band	Level	Grass	Vegetables	Wheat	CV of slopes
Far-red	Canopy	$y = 0.0065x + 0.122$ $R^2 = 0.7873$	$y = 0.017x - 0.5606$ $R^2 = 0.7078$	$y = 0.005x + 0.0213$ $R^2 = 0.9182$	0.688
	Leaf	$y = 0.0423x + 0.468$ $R^2 = 0.8567$	$y = 0.0778x - 2.3764$ $R^2 = 0.6803$	$y = 0.0352x + 0.1319$ $R^2 = 0.9292$	0.441
	PS	$y = 0.0634x + 0.8884$ $R^2 = 0.8786$	$y = 0.1108x - 3.0645$ $R^2 = 0.6122$	$y = 0.0495x + 0.6585$ $R^2 = 0.9227$	0.431
Red	Canopy	$y = 0.0035x + 0.1653$ $R^2 = 0.7068$	$y = 0.0074x + 0.0417$ $R^2 = 0.4672$	$y = 0.0033x + 0.0056$ $R^2 = 0.8232$	0.488
	Leaf	$y = 0.0336x + 0.9976$ $R^2 = 0.7621$	$y = 0.0444x + 0.9485$ $R^2 = 0.1964$	$y = 0.0292x + 0.4097$ $R^2 = 0.6182$	0.219
	PS	$y = 0.3808x + 10.094$ $R^2 = 0.7719$	$y = 0.5914x + 1.3347$ $R^2 = 0.4455$	$y = 0.358x + 1.031$ $R^2 = 0.6831$	0.290

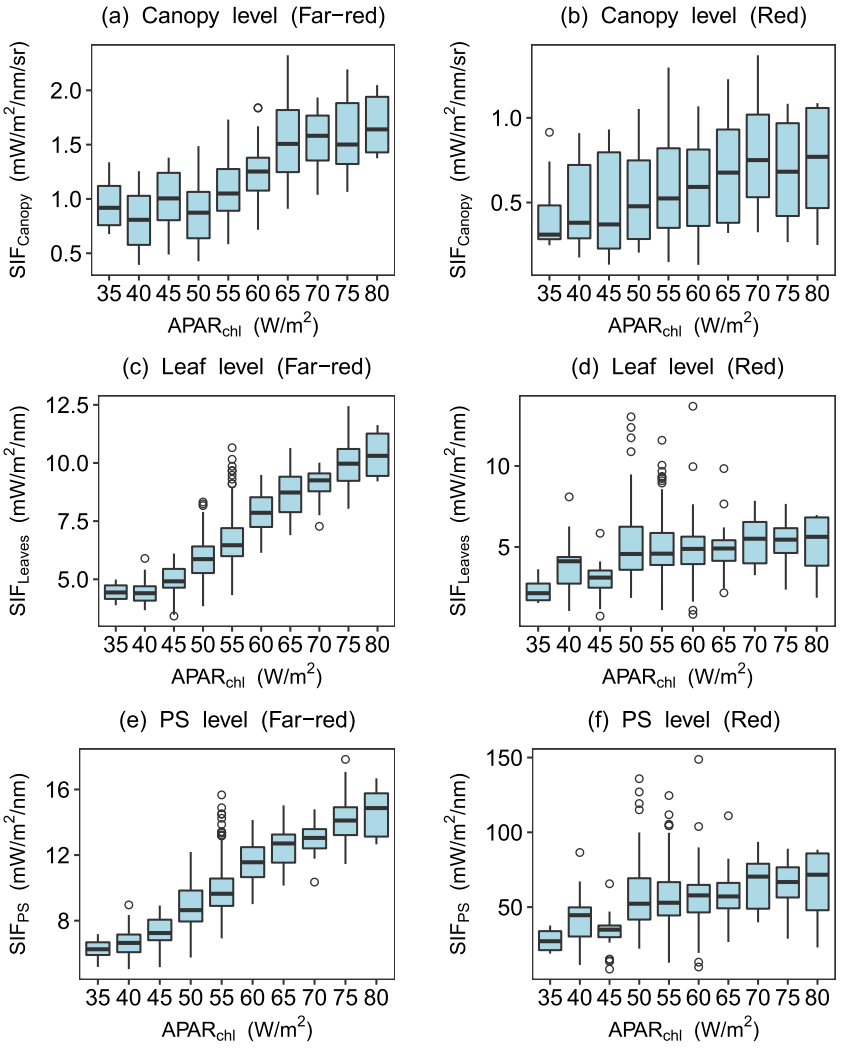

Fig. 10. The relationship between $APAR_{chl}$ and multi-angular observations of SIF at canopy level (a, b) and estimated SIF at leaf level (c, d) or PS level (e, f) by the RF approach. The bottom and top of the boxes correspond to the first and third quartiles, the thick horizontal line in each box is the median, the whiskers show the maximum/minimum values within 1.5 IQR, and the circles show the outliers that lie outside 1.5 IQR. The multi-angular observations were conducted on a wheat canopy. The averaged number of observations per APAR interval is 49.

at canopy level was efficiently corrected after the downscaling. For example, as shown in the image, despite a relative spatial visual homogeneity of *Field C* (see the true color image in Fig. 12), the map of SIF_{Canopy} showed a systematically increasing trend from west to east. The view zenith angle for *HyPlant* varied from −16.7° to ~ 16.7° for pixels from the left to the right of the swath and so this variation in SIF_{Canopy} within a homogeneous field may be related to SIF anisotropy. In contrast, the value of SIF_{PS} in this field was much more

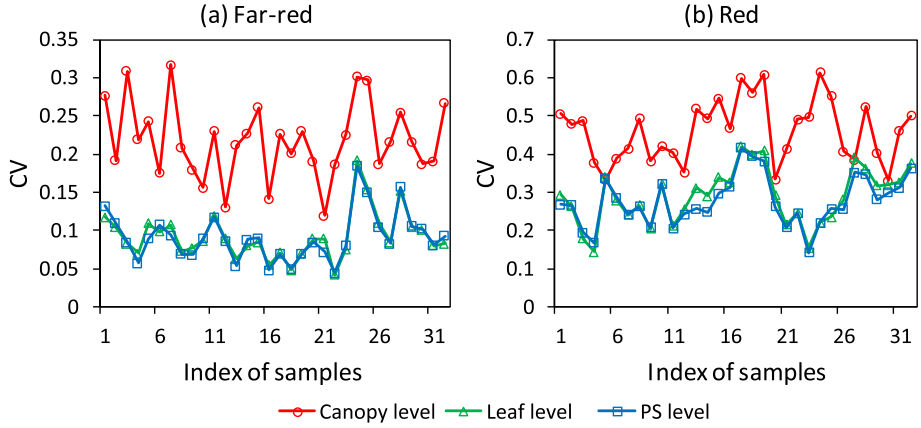

Fig. 11. The coefficients of variation (CV) of the observed canopy SIF and leaf or PS SIF estimated by the RF approach for each set of multi-angular observations in the solar principal plane. Each sample was calculated using a set of multi-angular observations taken within 7 min and the SIF at PS level was expected to be constant.

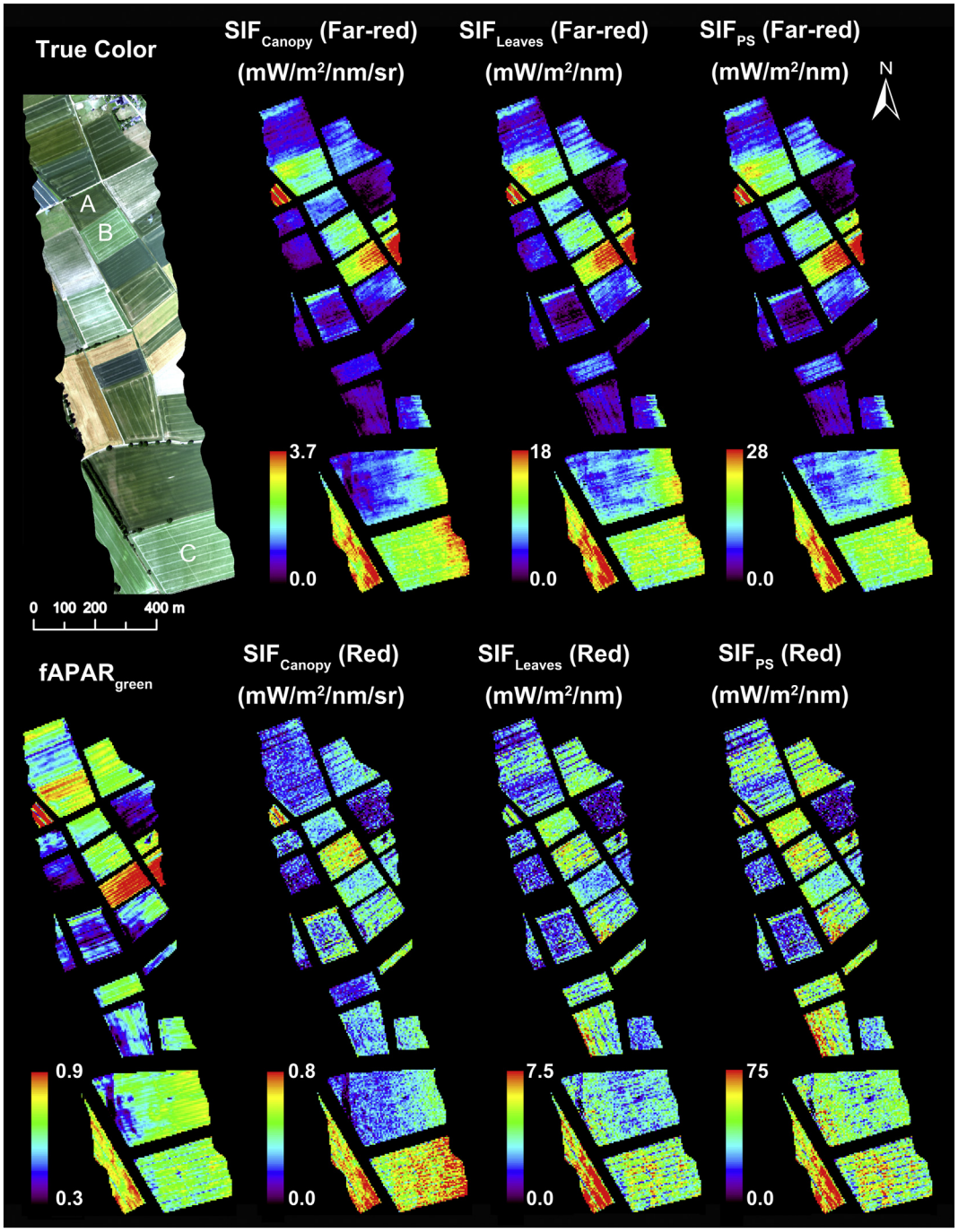

Fig. 12. True color composited *HyPlant* image and values of $fAPAR_{green}$, SIF at canopy level (retrieved using the iFLD method), SIF at leaf level and PS level (estimated using the RF approach) at both the far-red (760 nm) and red (687 nm) bands. The image was acquired at 14:58 (local time) on June 30, 2015 over the study area located in the Ruhr catchment in the central western part of North Rhine-Westphalia, Germany (50.864° N, 6.452° E). The flight height was 600 m above ground. The species in the fields labeled as "A", "B" and "C" in the true color image are winter wheat, potato and sugar beet, respectively. The three fields are selected as examples for further analysis. (For interpretation of the references to color in this figure legend, the reader is referred to the web version of this article.)

homogeneous.

Relationship between $fAPAR_{green}$ and SIF at canopy, leaf or PS level extracted from the *HyPlant* image vegetation pixels were presented in Fig. 13. Although the spatial resolution of the *HyPlant* image was reduced from 1 m to 5 m, the SIF images still appear noisy, especially for the red band. To further reduce the noise influence, we aggregated image pixels into 50 m × 50 m bins, in which the $fAPAR_{green}$ and SIF values were averaged (the scatter plots for the 5 m × 5 m images are available in the Supplementary materials (Fig. S3)). Since the *HyPlant* image used in this study was acquired within 1 min and the study area was flat, the PAR was expected to be constant for all pixels. The graphs showed a stronger and more linear relationship between SIF_{PS} and $fAPAR_{green}$ than between SIF_{Canopy} and $fAPAR_{green}$ for both the far-red band and the red band. The downscaling of SIF from canopy to PS level using the RF approach has increased the value of R^2 for the linear relationship between SIF and $fAPAR_{green}$ from 0.347 to 0.440 at the far-red band, and from 0.056 to 0.181 at the red band. For the far-red band, values of R^2 for the leaf level and PS level were very similar, while for the red band, the value of R^2 for the PS level was higher than that for the leaf level.

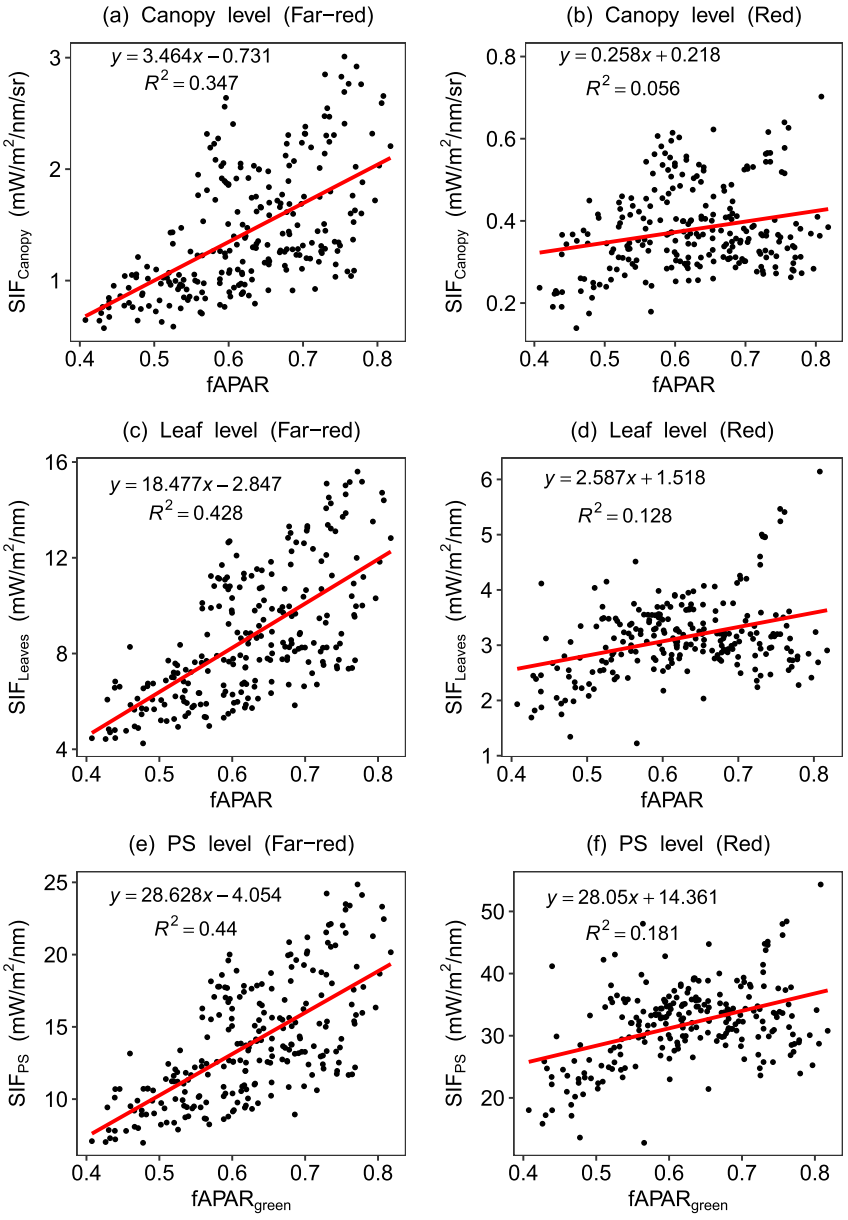

Fig. 13. Relationship between $fAPAR_{green}$ and SIF at canopy level, leaf level and PS level retrieved from the HyPlant image. Non-vegetation pixels were excluded. In order to reduce the propagation of noise, each point represents the averaged pixel value in a 50 m × 50 m window.

4. Discussion

4.1. Downscaling of SIF for the correction of SIF anisotropy

The observed SIF anisotropy at the canopy level is due to the re-absorption and scattering effects within the canopy. Guanter et al. (2012) and Joiner et al. (2012) reported the influence of the sun-view geometry on satellite remotely sensed SIF. Since the upwelling radiative transfer process from leaf level to canopy level for SIF emission is similar to that of reflected radiation, one can assume that SIF anisotropy is similar to that of reflectance (Liu et al., 2016).

According to the physical analysis of the SIF radiative transfer within the canopy conducted in this study, which was neglecting the influence of soil reflectance (is applicable for dense canopies), the SIF anisotropy at canopy level can be normalized by the BRF as expressed by Eq. (14), which is consistent with Liu et al. (2016). Multi-angular measurements of a winter wheat canopy were used in the evaluation of the SIF downscaling (Figs. 11 and 12). The results showed that, after the downscaling process, the difference in the values of SIF observed at different VZAs was reduced effectively. Similarly, in the *HyPlant* image, due to the variation of view zenith angle, SIF at canopy level showed obvious differences between the center and edges of the swath, while SIF at PS level was more homogeneous within each field.

Pinto et al. (2017) showed the angular distribution of SIF emission of a sugar beet canopy which consistent with our DART simulations shown in Fig. 1, and they pointed out that the directional SIF emission is related to the canopy structure. He et al. (2017) developed a model to normalize the remotely sensed SIF to the hot spot direction by quantifying the fraction of sunlit and shaded leaves in the field of view, and consequently, the total SIF at canopy level could be estimated as a weighted sum of SIF from sunlit and shaded leaves. They reported that the calculated total SIF was better related with the simulated total GPP than the original SIF observation. According to these relevant studies, the demonstrated SIF directional correction is especially important for long-term, ground-based or satellite-based observations of SIF time series as the sun-view geometry has a big influence on the SIF values

(Guanter et al., 2012; Joiner et al., 2012; Liu et al., 2016; He et al., 2017; Pinto et al., 2017). The downscaling approach proposed in this paper presents a practical method of reducing the anisotropy of SIF emissions, which consequently enables less biased understanding of the SIF information at canopy level.

4.2. Improvements of APAR estimation by SIF downscaling

APAR is a bridge linking SIF to GPP (Berry et al., 2012; Porcar-Castell et al., 2014). Besides the SIF anisotropy at the canopy level, the SIF-APAR relationship also depends on the canopy components and structures.

Du et al. (2017) studied the response of SIF to $APAR_{chl}$ using a simulated dataset and ground measurements, and found that the relationship between SIF_{Canopy} and $APAR_{chl}$ is highly dependent on the canopy structure and chlorophyll content, especially for the red band. Our study pointed out that corrections for the re-absorption and scattering that affects the SIF transfer from the PS level to canopy level is important for linking SIF_{Canopy} to $APAR_{chl}$. The study by Guanter et al. (2014) also found that there are differences between SIF-GPP models relationships for US croplands and European grasslands. According to the multi-species experiments used in our study (Fig. 10), the RF-based downscaling of SIF is efficient to reduce the influence of the re-absorption and scattering effects within the canopy, and to reduce the species-dependency of the SIF-$APAR_{chl}$ models.

Wieneke et al. (2016) analyzed the value of F_{yield} at canopy level (SIF_{Canopy}/APAR) for different agricultural fields captured in a *HyPlant* image, and found that F_{yield} varied with the crop type and with the time of image acquisition, i.e., the solar zenith and azimuth angles. The reason could be partly related to the re-absorption and scattering of SIF within the canopy. The results that we obtained using the *HyPlant* image further support the idea that SIF downscaling from canopy level to PS level can help to achieve more stable and reliable SIF-based APAR models.

4.3. The variation of SIF spectral shape at canopy, leaf and PS levels

Apart from the intensity of single-wavelength SIF, the spectral shape of SIF also contains important information (L. Liu et al., 2015; X. Liu et al., 2015). The two photosystems, PS I and PS II, contribute differently to the SIF emission. The PS II is responsible for the SIF emission at both the red and far-red bands, while the PS I only contributes to the far-red SIF emission and has a much smaller yield (Pfündel, 1998; Agati et al., 2000). Therefore, the spectral shape of SIF is related to the energy distribution between PS I and PS II (Porcar-Castell et al., 2014). However, as the within-canopy re-absorption and scattering effects on SIF are quite different for the red band and the far-red band, the spectral shape of SIF at canopy, leaf and PS levels varies significantly (Fournier et al., 2012; Moya et al., 2006; Porcar-Castell et al., 2014). Romero et al. (2018) developed a model based on the canopy reflectance, canopy transmittance and soil reflectance to retrieve the spectral shape of fluorescence emission at leaf level from the observed fluorescence at canopy level. Ramos and Lagorio (2004) proposed a physical model to obtain the fluorescence spectra at PS level by combining the leaf fluorescence emission and leaf reflectance. Based on the two studies above, it is possible to retrieve the SIF spectral shape at PS level from SIF observation at canopy level, but the absolute intensity of SIF emission at leaf level or PS level is not available.

In this paper, although we focused on the SIF downscaling at two spectrally narrow bands instead of full-wavelength, it is still possible to see the variation of SIF spectral shape at canopy, leaf and PS levels using the ratio of far-red and red SIF. For the wheat canopy introduced in the multi-species experiment, the averaged ratios of SIF at the far-red band (760 nm) and red band (687 nm) are 1.63, 1.17 and 0.17 for the canopy level, leaf level and PS level, respectively. The significant decrease of the SIF ratios results from a much stronger re-absorption effect at the red band. The results are consistent with the Fig. 8 in Romero et al. (2018).

4.4. Reliability of this study

A practical solution based on RF regression was proposed to overcome the difficulties in the physical approach for SIF downscaling from canopy level to PS level. As an efficient machine learning algorithm, the RF regression model is able to give accurate prediction of parameters if it is properly trained. The RF model is made up of a large number of decision trees. Each decision tree is independently grown on a bootstrap sample, and hence, the trees are weakly correlated. Therefore, the risk of overfitting the training dataset, which is a significant problem for many machine learning algorithms, can be reduced (Abdel-Rahman et al., 2013). The RF model is a black box and is totally reliant on the training dataset, which may reduce its robustness and applicability under certain conditions. For comparison, a simple multiple linear regression (MLR) method was also tested using the SCOPE simulation, but the results (Fig. S4 in the Supplementary materials) were much worse than the RF model (as shown in Fig. 7), which confirmed that the RF model was more efficient to estimate the SIF escape probability based on the information from reflectance.

A physical analysis based on the spectral invariant theory was carried out to improve the robustness of the SIF downscaling model and find out the most important variables. However, there are some limitations remaining in using the spectral invariant theory. In the spectral invariant theory, the leaf reflectance and transmittance are combined as the leaf single scattering albedo. In other words, the different transfer processes of the photons scattered downwards and upwards by leaves were ignored. Yang and Van der Tol (2018) analyzed the radiative transfer of incident light and emitted SIF considering the leaf reflectance and transmittance separately and got the same equation as Eq. (14). But they pointed out that the equation was not valid for the red band due to the difference between the leaf reflectance and transmittance. At the far-red band, the influence of the difference of leaf reflectance and transmittance becomes relatively small with the increasing interaction order. At the red band, however, the difference of leaf reflectance and transmittance is not ignorable because the single scattering dominates. Nevertheless, Yang and Van der Tol (2018) also found that the ε_{CL} and $\frac{BRF}{i_0\omega_L}$ were still proportional at the red band for individual leaves, but the slope of the relationship was influenced by the leaf structure and pigment composition. In our study, we did not rely on the physical analysis for SIF downscaling, but only used the spectral invariant theory to find out the key parameters to estimate the SIF escape probability. Therefore, the results of this study were not directly influenced by the limitations of the spectral invariant theory, and the SIF downscaling at the red band was still reasonable and valid, although the accuracy was lower than that at the far-red band.

We used different data stemming from models, field and airborne observations to assess reliability of our approach. Although we could demonstrate consistency of downscaling results across levels and experiments, particularly results obtained from *HyPlant* data were less clear compared to modelling results. This is expected and related to the wealth of factors determining real measurements. Further, the atmospheric correction of airborne measured radiance data to retrieve surface reflectance and eventually calculate vegetation products such as fAPAR is a highly complex task. Particularly canopy structure can introduce uncertainties in estimated irradiance due to varying fractions of diffuse and direct irradiance components, thus causing errors in retrieved vegetation products (Damm et al., 2015b).

Other assumptions applied might also limit the scope of our analysis. i) The training dataset was simulated with the SCOPE model. SCOPE provides relatively reliable simulations of SIF at PS, leaf and canopy levels, and has been widely used in studies dealing with SIF (Damm et al., 2015a, Verrelst et al., 2016). However, SCOPE is a 1-D

model and its simulations may only be reliable for canopies with a relatively simple structure, such as crops and grass, and not for more complicated canopies such as forest. The clumping effect was also neglected in the physical analysis. The performance of the proposed method for the cases across canopies still needs to be further tested. ii) The estimated SIF at PS level is not possible to be directly validated for ground or airborne measurements. $APAR_{chl}$ or $fAPAR_{green}$ were, therefore, used to indirectly evaluate the reliability of estimated SIF_{PS}. But the measurements or estimates of $APAR_{chl}$ or $fAPAR_{green}$ also contain uncertainties. Moreover, the influence of SIF yield was neglected. Therefore, the validation of our SIF downscaling must be elaborated in future work.

5. Conclusions

Remote sensing based SIF measurements at canopy level are largely affected by re-absorption and scattering within the leaves and canopies, so the downscaling of SIF from canopy level to PS level is important to better understand the link between SIF and GPP. A practicable solution based on physical analysis and RF regression for the estimation of SIF escape probability was proposed. The RF regression model was trained using SCOPE simulations. The results were evaluated using SCOPE and DART simulations, field experiments and *HyPlant* image. The results indicate that, for the far-red band, the SIF escape probability is dominated by the canopy scattering, while for the red band, the SIF escape probability is related to both canopy scattering and reabsorption within leaves. We conclude that accurate knowledge and correction of SIF escape probability is essential to reduce associated large uncertainty in the SIF-APAR relationship, and this is also expected to improve the SIF-based GPP estimation. Our suggested approach is based on the spectral invariant theory and relies on canopy directional reflectance at the red, red-edge and far-red bands to downscale canopy SIF to leaf or photosystem level. Although we could successfully demonstrate the reliability of our approach, we identified strong sensitivity of our results to data quality and assumptions in underlying models. We suggest advancing reliability of reflectance data retrievals in requested wavelength ranges and further assessing the impact of assumptions underlying our analysis.

Acknowledgements

The authors gratefully acknowledge the financial support provided by the National Key R&D Program of China (2017YFA0603001) and the National Natural Science Foundation of China (41701396, 41671349). L.G. has been supported by the Emmy Noether Programme of the German Research Foundation (GU 1276/1-1). Z.M. has been supported by the Australian Research Council Future Fellowship project (FT160100477). X.L. has been supported by the Sino-German (CSC-DAAD) Postdoc Scholarship Program for his work in Germany. Acquisition of the *HyPlant* images and data processing was supported by the European Space Agency (ESA) in the frame of the HyFLEX campaign (ESA contract no. 4000107143/12/NL/FF/If CCN3), the SFB/TR 32 “Patterns in Soil-Vegetation-Atmosphere Systems: Monitoring, Modelling, and Data Assimilation”—subproject D2 (www.tr32.de), funded by the Deutsche Forschungsgemeinschaft (DFG) and the German Plant Phenotyping Network (DPPN; Förderkennzeichen 031A053A/B/C) of the BMBF. Additional financial support was provided by the Forschungszentrum Jülich GmbH supporting the development and operation of *HyPlant*. The authors thank Dr. Christiaan Van der Tol for providing the SCOPE code, and thank Prof. Anatoly Gitelson for providing helpful suggestions in relation to fAPAR estimation, and Patrick Rademske for supports related to providing the *HyPlant* dataset. The authors also thank the editor and anonymous reviewers for their detailed and constructive suggestions for improving the manuscript.

Appendix A. Supplementary data

Supplementary data to this article can be found online at https://doi.org/10.1016/j.rse.2018.05.035.

References

Abdel-Rahman, E.M., Ahmed, F.B., Ismail, R., 2013. Random forest regression and spectral band selection for estimating sugarcane leaf nitrogen concentration using EO-1 Hyperion hyperspectral data. Int. J. Remote Sens. 34, 712–728.

Ač, A., Malenovský, Z., Olejníčková, J., Gallé, A., Rascher, U., Mohammed, G., 2015. Meta-analysis assessing potential of steady-state chlorophyll fluorescence for remote sensing detection of plant water, temperature and nitrogen stress. Remote Sens. Environ. 168, 420–436.

Adams, W.W., Winter, K., Schreiber, U., Schramel, P., 1990. Photosynthesis and chlorophyll fluorescence characteristics in relationship to changes in pigment and element composition of leaves of *Platanus occidentalis* L. during autumnal leaf senescence. Plant Physiol. 92, 1184–1190.

Agati, G., Fusi, F., Mazzinghi, P., Paola, M.L.D., 1993. A simple approach to the evaluation of the reabsorption of chlorophyll fluorescence spectra in intact leaves. J. Photochem. Photobiol. B 17 (2), 163–171.

Agati, G., Cerovic, Z.G., Moya, I., 2000. The effect of decreasing temperature up to chilling values on the in vivo F685/F735 chlorophyll fluorescence ratio in *Phaseolus vulgaris* and Pisum sativum: the role of the photosystem I contribution to the 735 nm fluorescence band. Photochem. Photobiol. 72 (1), 75–84.

Alonso, L., Gomez-Chova, L., Vila-Frances, J., Amoros-Lopez, J., Guanter, L., Calpe, J., Moreno, J., 2008. Improved Fraunhofer Line Discrimination method for vegetation fluorescence quantification. IEEE Geosci. Remote Sens. Lett. 5, 620–624.

Berry, J.A., Frankenberg, C., Wennberg, P., Baker, I., Bowman, K.W., Castro-Contreas, S., Cendrero-Mateo, M.P., Damm, A., Drewry, D., Ehlmann, B., 2012. New methods for measurement of photosynthesis from space. Geophys. Res. Lett. 38, L17706.

Breiman, L., 2001. Random forests. Mach. Learn. 45, 5–32.

Burkart, A., Schickling, A., Pilar Cendrero Mateo, M., Wrobel, T., Rossini, M., Cogliati, S., Julitta, T., Rascher, U., 2015. A method for uncertainty assessment of passive sun-induced chlorophyll fluorescence retrieval by using an infrared reference light. IEEE Sensors 15, 4603–4611.

Chen, J.M., Black, T., 1992. Defining leaf area index for non-flat leaves. Plant Cell Environ. 15, 421–429.

Clevers, J.G., Gitelson, A.A., 2013. Remote estimation of crop and grass chlorophyll and nitrogen content using red-edge bands on sentinel-2 and-3. Int. J. Appl. Earth Obs. Geoinf. 23, 344–351.

Cogliati, S., Rossini, M., Julitta, T., Meroni, M., Schickling, A., Burkart, A., Pinto, F., Rascher, U., Colombo, R., 2015. Continuous and long-term measurements of reflectance and sun-induced chlorophyll fluorescence by using novel automated field spectroscopy systems. Remote Sens. Environ. 164, 270–281.

Colwell, J.E., 1974. Vegetation canopy reflectance. Remote Sens. Environ. 3, 175–183.

Coops, N.C., Hilker, T., Hall, F.G., Nichol, C.J., Drolet, G.G., 2010. Estimation of light-use efficiency of terrestrial ecosystems from space: a status report. Bioscience 60, 788–797.

Cordón, G.B., Lagorio, M.G., 2006. Re-absorption of chlorophyll fluorescence in leaves revisited. A comparison of correction models. Photochem. Photobiol. Sci. 5 (8), 735–740.

Damm, A., Erler, A., Hillen, W., Meroni, M., Schaepman, M.E., Verhoef, W., Rascher, U., 2011. Modeling the impact of spectral sensor configurations on the FLD retrieval accuracy of sun-induced chlorophyll fluorescence. Remote Sens. Environ. 115, 1882–1892.

Damm, A., Guanter, L., Laurent, V.C.E., Schaepman, M.E., Schickling, A., Rascher, U., 2014. FLD-based retrieval of sun-induced chlorophyll fluorescence from medium spectral resolution airborne spectroscopy data. Remote Sens. Environ. 147, 256–266.

Damm, A., Guanter, L., Paul-Limoges, E., Van der Tol, C., Hueni, A., Buchmann, N., Eugster, W., Ammann, C., Schaepman, M.E., 2015a. Far-red sun-induced chlorophyll fluorescence shows ecosystem-specific relationships to gross primary production: an assessment based on observational and modeling approaches. Remote Sens. Environ. 166, 91–105.

Damm, A., Guanter, L., Verhoef, W., Schläpfer, D., Garbari, S., Schaepman, M.E., 2015b. Impact of varying irradiance on vegetation indices and chlorophyll fluorescence derived from spectroscopy data. Remote Sens. Environ. 156, 202–215.

Dash, J., Curran, P., 2004. The MERIS terrestrial chlorophyll index. Int. J. Remote Sens. 25, 5403–5413.

Daumard, F., Goulas, Y., Champagne, S., Fournier, A., Ounis, A., Olioso, A., Moya, I., 2012. Continuous monitoring of canopy level sun-induced chlorophyll fluorescence during the growth of a Sorghum field. IEEE Trans. Geosci. Remote Sens. 1–9.

Du, S., Liu, L., Liu, X., Hu, J., 2017. Response of canopy solar-induced chlorophyll fluorescence to the absorbed photosynthetically active radiation absorbed by chlorophyll. Remote Sens. 9, 911.

Field, C.B., Behrenfeld, M.J., Randerson, J.T., Falkowski, P., 1998. Primary production of the biosphere: integrating terrestrial and oceanic components. Science 281, 237–240.

Fournier, A., Daumard, F., Champagne, S., Ounis, A., Goulas, Y., Moya, I., 2012. Effect of canopy structure on sun-induced chlorophyll fluorescence. ISPRS J. Photogramm. Remote Sens. 68, 112–120.

Frankenberg, C., Fisher, J.B., Worden, J., Badgley, G., Saatchi, S.S., Lee, J.-E., Toon, G.C., Butz, A., Jung, M., Kuze, A., Yokota, T., 2011. New global observations of the terrestrial carbon cycle from GOSAT: patterns of plant fluorescence with gross primary productivity. Geophys. Res. Lett. 38.

Gastellu-Etchegorry, J.-P., Yin, T., Lauret, N., Cajgfinger, T., Gregoire, T., Grau, E., Feret, J.-B., Lopes, M., Guilleux, J., Dedieu, G., 2015. Discrete anisotropic radiative transfer (DART 5) for modeling airborne and satellite spectroradiometer and LIDAR acquisitions of natural and urban landscapes. Remote Sens. 7, 1667–1701.

Gastellu-Etchegorry, J.-P., Lauret, N., Yin, T., Landier, L., Kallel, A., Malenovský, Z., Al Bitar, A., Aval, J., Benhmida, S., Qi, J., 2017. DART: recent advances in remote sensing data modeling with atmosphere, polarization, and chlorophyll fluorescence. IEEE J. Sel. Top. Appl. Earth Obs. Remote Sens. 10, 2640–2649.

Gitelson, A.A., Buschmann, C., Lichtenthaler, H.K., 1998. Leaf chlorophyll fluorescence corrected for re-absorption by means of absorption and reflectance measurements. J. Plant Physiol. 152, 283–296.

Gitelson, A.A., Vina, A., Ciganda, V., Rundquist, D.C., Arkebauer, T.J., 2005. Remote estimation of canopy chlorophyll content in crops. Geophys. Res. Lett. 32.

Gitelson, A.A., Peng, Y., Huemmrich, K.F., 2014. Relationship between fraction of radiation absorbed by photosynthesizing maize and soybean canopies and NDVI from remotely sensed data taken at close range and from MODIS 250 m resolution data. Remote Sens. Environ. 147, 108–120.

Grossmanna, K., 2014. PhotoSpec-ground-based remote sensing of solar-induced chlorophyll fluorescence. J. Exp. Bot. 22, 095.

Guanter, L., Frankenberg, C., Dudhia, A., Lewis, P.E., Gómez-Dans, J., Kuze, A., ... Grainger, R.G., 2012. Retrieval and global assessment of terrestrial chlorophyll fluorescence from GOSAT space measurements. Remote Sens. Environ. 121, 236–251.

Guanter, L., Zhang, Y., Jung, M., Joiner, J., Voigt, M., Berry, J.A., Frankenberg, C., Huete, A.R., Zarco-Tejada, P., Lee, J.-E., 2014. Global and time-resolved monitoring of crop photosynthesis with chlorophyll fluorescence. Proc. Natl. Acad. Sci. 201320008.

He, L., Chen, J.M., Liu, J., Mo, G., Joiner, J., 2017. Angular normalization of GOME-2 sun-induced chlorophyll fluorescence observation as a better proxy of vegetation productivity. Geophys. Res. Lett. 44 (11), 5691–5699.

Huang, D., Knyazikhin, Y., Dickinson, R.E., Rautiainen, M., Stenberg, P., Disney, M., Lewis, P., Cescatti, A., Tian, Y., Verhoef, W., 2007. Canopy spectral invariants for remote sensing and model applications. Remote Sens. Environ. 106, 106–122.

Jacquemoud, S., Baret, F., 1990. PROSPECT: a model of leaf optical properties spectra. Remote Sens. Environ. 34, 75–91.

Joiner, J., Yoshida, Y., Vasilkov, A.P., Corp, L.A., Middleton, E.M., 2011. First observations of global and seasonal terrestrial chlorophyll fluorescence from space. Biogeosciences 8, 637–651.

Joiner, J., Yoshida, Y., Vasilkov, A.P., Middleton, E.M., Campbell, P.K.E., Kuze, A., 2012. Filling-in of near-infrared solar lines by terrestrial fluorescence and other geophysical effects: simulations and space-based observations from SCIAMACHY and GOSAT. Atmos. Meas. Tech. 5, 809–829.

Joiner, J., Guanter, L., Lindstrot, R., Voigt, M., Vasilkov, A.P., Middleton, E.M., Huemmrich, K.F., Yoshida, Y., Frankenberg, C., 2013. Global monitoring of terrestrial chlorophyll fluorescence from moderate spectral resolution near-infrared satellite measurements: methodology, simulations, and application to GOME-2. Atmos. Meas. Tech. 6, 2803–2823.

Jordan, C.F., 1969. Derivation of leaf-area index from quality of light on the forest floor. Ecology 50, 663–666.

Knyazikhin, Y., Kranigk, J., Myneni, R.B., Panfyorov, O., Gravenhorst, G., 1998. Influence of small-scale structure on radiative transfer and photosynthesis in vegetation canopies. J. Geophys. Res. Atmos. 103, 6133–6144.

Knyazikhin, Y., Schull, M.A., Xu, L., Myneni, R.B., Samanta, A., 2011. Canopy spectral invariants. Part 1: a new concept in remote sensing of vegetation. J. Quant. Spectrosc. Radiat. Transf. 112 (4), 727–735.

Knyazikhin, Y., Schull, M.A., Stenberg, P., Mõttus, M., Rautiainen, M., Yang, Y., Marshak, A., Carmona, P.L., Kaufmann, R.K., Lewis, P., 2013. Hyperspectral remote sensing of foliar nitrogen content. Proc. Natl. Acad. Sci. 110, E185–E192.

Köhler, P., Guanter, L., Joiner, J., 2015. A linear method for the retrieval of sun-induced chlorophyll fluorescence from GOME-2 and SCIAMACHY data. Atmos. Meas. Tech. 8, 2589–2608.

Liu, L.Y., Zhang, Y.J., Wang, J.H., Zhao, C.J., 2005. Detecting solar-induced chlorophyll fluorescence from field radiance spectra based on the Fraunhofer line principle. IEEE Trans. Geosci. Remote Sens. 43, 827–832.

Liu, L., Peng, D., Hu, Y., Jiao, Q., 2013. A novel in situ FPAR measurement method for low canopy vegetation based on a digital camera and reference panel. Remote Sens. 5, 274–281.

Liu, L., Liu, X., Hu, J., 2015. Effects of spectral resolution and SNR on the vegetation solar-induced fluorescence retrieval using FLD-based methods at canopy level. Eur. J. Remote. Sens. 48, 743–762.

Liu, X., Liu, L., Zhang, S., Zhou, X., 2015. New spectral fitting method for full-spectrum solar-induced chlorophyll fluorescence retrieval based on principal components analysis. Remote Sens. 7 (8), 10626–10645.

Liu, L., Liu, X., Wang, Z., Zhang, B., 2016. Measurement and analysis of bidirectional SIF emissions in wheat canopies. IEEE Trans. Geosci. Remote Sens. 54, 2640–2651.

Liu, L., Guan, L., Liu, X., 2017a. Directly estimating diurnal changes in GPP for C3 and C4 crops using far-red sun-induced chlorophyll fluorescence. Agric. For. Meteorol. 232, 1–9.

Liu, L., Liu, X., Hu, J., Guan, L., 2017b. Assessing the wavelength-dependent ability of solar-induced chlorophyll fluorescence to estimate the GPP of winter wheat at the canopy level. Int. J. Remote Sens. 38, 4396–4417.

Ma, C., Zhang, H.H., Wang, X., 2014. Machine learning for big data analytics in plants. Trends Plant Sci. 19 (12), 798–808.

Maier, S.W., Günther, K.P., Stellmes, M., 2003. Sun-induced fluorescence: a new tool for precision farming. In: McDonald, M., Schepers, J., Tartly, L., Toai, T.V., Major, D. (Eds.), Digital Imaging and Spectral Techniques: Applications to Precision Agriculture and Crop Physiology. American Society of Agronomy Special Publication, Madison, WI, USA, pp. 209–222.

Malenovský, Z., Mishra, K.B., Zemek, F., Rascher, U., Nedbal, L., 2009. Scientific and technical challenges in remote sensing of plant canopy reflectance and fluorescence. J. Exp. Bot. 60 (11), 2987–3004.

Malenovský, Z., Homolová, L., Zurita-Milla, R., Lukeš, P., Kaplan, V., Hanuš, J., Gastellu-Etchegorry, J.-P., Schaepman, M.E., 2013. Retrieval of spruce leaf chlorophyll content from airborne image data using continuum removal and radiative transfer. Remote Sens. Environ. 131, 85–102.

Meroni, M., Busetto, L., Colombo, R., Guanter, L., Moreno, J., Verhoef, W., 2010. Performance of spectral fitting methods for vegetation fluorescence quantification. Remote Sens. Environ. 114, 363–374.

Migliavacca, M., Perez-Priego, O., Rossini, M., El-Madany, T.S., Moreno, G., Van der Tol, C., Rascher, U., Berninger, A., Bessenbacher, V., Burkart, A., 2017. Plant functional traits and canopy structure control the relationship between photosynthetic CO2 uptake and far-red sun-induced fluorescence in a Mediterranean grassland under different nutrient availability. New Phytol. 214, 1078–1091.

Monteith, J., 1972. Solar radiation and productivity in tropical ecosystems. J. Appl. Ecol. 9 (3), 747–766.

Monteith, J.L., Moss, C., 1977. Climate and the efficiency of crop production in Britain. Philos. Trans. R. Soc. Lond. Ser. B Biol. Sci. 281 (980), 277–294.

Moya, I., Cerovic, Z.G., 2004. Remote sensing of chlorophyll fluorescence: instrumentation and analysis. In: Papageorgiou, G.C., Govindgee (Eds.), Chlorophyll *a* Fluorescence. Springer, Kluwer, Dordrecht, pp. 429–445.

Moya, I., Daumard, F., Moise, N., Ounis, A., Goulas, Y., 2006. First airborne multiwavelength passive chlorophyll fluorescence measurements over La Mancha (Spain) fields. Second Recent Adv. Quant. Remote Sens. 820–825.

Nilson, T., 1971. A theoretical analysis of the frequency of gaps in plant stands. Agric. Meteorol. 8, 25–38.

Pfündel, E., 1998. Estimating the contribution of photosystem I to total leaf chlorophyll fluorescence. Photosynth. Res. 56 (2), 185–195.

Pinto, F., Müller-Linow, M., Schickling, A., Cendrero-Mateo, M.P., Ballvora, A., Rascher, U., 2017. Multiangular observation of canopy sun-induced chlorophyll fluorescence by combining imaging spectroscopy and stereoscopy. Remote Sens. 9 (5), 415.

Plascyk, J.A., 1975. The MK II Fraunhofer line discriminator (FLD-II) for airborne and orbital remote sensing of solar-stimulated luminescence. Opt. Eng. 14, 339–346.

Porcar-Castell, A., Tyystjärvi, E., Atherton, J., Van der Tol, C., Flexas, J., Pfündel, E.E., Moreno, J., Frankenberg, C., Berry, J.A., 2014. Linking chlorophyll a fluorescence to photosynthesis for remote sensing applications: mechanisms and challenges. J. Exp. Bot. eru191.

Ramos, M.E., Lagorio, M.G., 2004. True fluorescence spectra of leaves. Photochem. Photobiol. Sci. 3, 1063–1066.

Rascher, U., Alonso, L., Burkart, A., Cilia, C., Cogliati, S., Colombo, R., Damm, A., Drusch, M., Guanter, L., Hanus, J., 2015. Sun-induced fluorescence–a new probe of photosynthesis: first maps from the imaging spectrometer HyPlant. Glob. Chang. Biol. 21, 4673–4684.

Romero, J.M., Cordon, G.B., Lagorio, M.G., 2018. Modeling re-absorption of fluorescence from the leaf to the canopy level. Remote Sens. Environ. 204, 138–146.

Ross, J., 2012. The Radiation Regime and Architecture of Plant Stands. Springer Science & Business Media.

Rouse, J., Haas, R., Schell, J., Deering, D., 1973. Monitoring vegetation systems in the Great Plains with ERTS (Earth Resources Technology Satellite). In: Proceedings of 3rd ERTS Symposium, pp. 48–62.

Ryu, Y., Sonnentag, O., Nilson, T., Vargas, R., Kobayashi, H., Wenk, R., Baldocchi, D.D., 2010. How to quantify tree leaf area index in an open savanna ecosystem: a multi-instrument and multi-model approach. Agric. For. Meteorol. 150, 63–76.

Sims, D.A., Gamon, J.A., 2002. Relationships between leaf pigment content and spectral reflectance across a wide range of species, leaf structures and developmental stages. Remote Sens. Environ. 81, 337–354.

Smolander, S., Stenberg, P., 2005. Simple parameterizations of the radiation budget of uniform broadleaved and coniferous canopies. Remote Sens. Environ. 94, 355–363.

Soudani, K., Hmimina, G., Delpierre, N., Pontailler, J.-Y., Aubinet, M., Bonal, D., Caquet, B., De Grandcourt, A., Burban, B., Flechard, C., 2012. Ground-based network of NDVI measurements for tracking temporal dynamics of canopy structure and vegetation phenology in different biomes. Remote Sens. Environ. 123, 234–245.

Stenberg, P., Mõttus, M., Rautiainen, M., 2016. Photon recollision probability in modelling the radiation regime of canopies—a review. Remote Sens. Environ. 183, 98–108.

Sun, Y., Frankenberg, C., Wood, J.D., Schimel, D., Jung, M., Guanter, L., Drewry, D., Verma, M., Porcar-Castell, A., Griffis, T.J., 2017. OCO-2 advances photosynthesis observation from space via solar-induced chlorophyll fluorescence. Science 358, eaam5747.

Van der Tol, C., Verhoef, W., Timmermans, J., Verhoef, A., Su, Z., 2009. An integrated model of soil-canopy spectral radiances, photosynthesis, fluorescence, temperature and energy balance. Biogeosciences 6, 3109–3129.

Van der Tol, C., Berry, J.A., Campbell, P.K.E., Rascher, U., 2014. Models of fluorescence and photosynthesis for interpreting measurements of solar-induced chlorophyll fluorescence. J. Geophys. Res. Biogeosci. 119 (12), 2312–2327.

Van Wittenberghe, S., Alonso, L., Verrelst, J., Moreno, J., Samson, R., 2015. Bidirectional sun-induced chlorophyll fluorescence emission is influenced by leaf structure and light scattering properties—a bottom-up approach. Remote Sens. Environ. 158, 169–179.

Verhoef, W., 1984. Light scattering by leaf layers with application to canopy reflectance modeling: the SAIL model. Remote Sens. Environ. 16 (2), 125–141.

Verrelst, J., Rivera, J.P., Van der Tol, C., Magnani, F., Mohammed, G., Moreno, J., 2015. Global sensitivity analysis of the SCOPE model: what drives simulated canopy-leaving sun-induced fluorescence. Remote Sens. Environ. 166 (8-2).

Verrelst, J., van der Tol, C., Magnani, F., Sabater, N., Rivera, J.P., Mohammed, G., Moreno, J., 2016. Evaluating the predictive power of sun-induced chlorophyll

fluorescence to estimate net photosynthesis of vegetation canopies: A SCOPE modeling study. Remote Sens. Environ. 176, 139–151.
Vilfan, N., Van der Tol, C., Muller, O., Rascher, U., Verhoef, W., 2016. Fluspect-B: a model for leaf fluorescence, reflectance and transmittance spectra. Remote Sens. Environ. 186, 596–615.
Viña, A., Gitelson, A.A., 2005. New developments in the remote estimation of the fraction of absorbed photosynthetically active radiation in crops. Geophys. Res. Lett. 32.
Wang, Y., Buermann, W., Stenberg, P., Smolander, H., Häme, T., Tian, Y., Hu, J., Knyazikhin, Y., Myneni, R.B., 2003. A new parameterization of canopy spectral response to incident solar radiation: case study with hyperspectral data from pine dominant forest. Remote Sens. Environ. 85, 304–315.
Wieneke, S., Ahrends, H., Damm, A., Pinto, F., Stadler, A., Rossini, M., Rascher, U., 2016. Airborne based spectroscopy of red and far-red sun-induced chlorophyll fluorescence: implications for improved estimates of gross primary productivity. Remote Sens. Environ. 184, 654–667.
Wyber, R., Malenovský, Z., Ashcroft, M.B., Osmond, B., Robinson, S.A., 2017. Do daily and seasonal trends in leaf solar induced fluorescence reflect changes in photosynthesis, growth or light exposure? Remote Sens. 9 (6), 604.
Yan, G., Ren, H., Hu, R., Yan, K., Zhang, W., 2012. A portable multi-angle observation system. In: Geoscience and Remote Sensing Symposium (IGARSS), 2012 IEEE International. IEEE, pp. 6916–6919.
Yang, P., Van der Tol, C., 2018. Linking canopy scattering of far-red sun-induced chlorophyll fluorescence with reflectance. Remote Sens. Environ. 209, 456–467.
Yang, X., Tang, J., Mustard, J.F., Lee, J.-E., Rossini, M., Joiner, J., Munger, J.W., Kornfeld, A., Richardson, A.D., 2015. Solar-induced chlorophyll fluorescence correlates with canopy photosynthesis on diurnal and seasonal scales in a temperate deciduous forest. Geophys. Res. Lett. 2015GL063201.
Zarco-Tejada, P.J., Catalina, A., González, M.R., Martín, P., 2013. Relationships between net photosynthesis and steady-state chlorophyll fluorescence retrieved from airborne hyperspectral imagery. Remote Sens. Environ. 136, 247–258.
Zhang, Y., Guanter, L., Berry, J.A., Van der Tol, C., Yang, X., Tang, J., Zhang, F., 2016. Model-based analysis of the relationship between sun-induced chlorophyll fluorescence and gross primary production for remote sensing applications. Remote Sens. Environ. 187, 145–155.